

INVESTIGATION OF END-BURNING TYPE HYBRID  
ROCKET MOTOR DOPED WITH HIGH ENTROPY  
ALLOY

BY

MUHAMMAD EZAMUDDIN EZZAD BIN SABRI

A thesis submitted in fulfilment of the requirement for the  
degree of Master of Science in Engineering

Kulliyyah of Engineering  
International Islamic University Malaysia

OCTOBER 2023

## ABSTRACT

Hybrid rocket motors (HRMs) have become an attractive propulsion system due to their advantages over solid and liquid rockets, such as safety, environmental friendliness, low cost, and typically not containing toxic additives. However, low regression rate and poor combustion efficiency are critical weaknesses that affects the performance. To address this issue, extensive investigations have been conducted on the end-burning hybrid rocket (EBHR) doped with high entropy alloys (HEAs) to improve the regression rate and increase combustion efficiency. Static firings were conducted to obtain the thrust, regression rate and specific impulse. Simulations were also performed using NASA CEA software to assess HEAs' performance in HRMs. The characteristic velocity, specific impulse, and adiabatic flame temperature were the propulsive parameters analyzed. The present investigation focuses on a single port EBHR utilizing paraffin wax doped with HEAs as the fuel. Experimental results showed that the inclusion of 5% HEAs contributed to a 45.4% increase in the regression rate, 28.03% increase in thrust, and 25.89% increase in specific impulse compared to pure paraffin wax. The EBHR demonstrated an overall lower performance compared to the conventional HRM due to unstable combustion throughout the firings. According to the simulations, the higher the HEAs' concentration, the better it performs at an oxidiser-to-fuel ratio (O/F) of 1.0-1.3. Gaseous oxygen (GOX) as the oxidiser provides the best performance overall but hydrogen peroxide (H<sub>2</sub>O<sub>2</sub>) performs better at O/F greater than 4. The experiments and simulations demonstrate the potential of HEAs to enhance the regression rate, thrust, and specific impulse of HRMs. End-burning has also shown no fluctuations of O/F and chamber pressure during steady-state, which might be helpful in some applications. The findings also highlight the influence of initial fuel mass, mass flux, and HEAs' concentration on the hybrid rocket's performance. These improvements can expand the range of applications for hybrid rockets and contribute to the growth of commercial space activities, scientific research, and space exploration efforts.

## ملخص البحث

أصبحت محركات الصواريخ الهجينة نظام دفع جذابًا نظرًا لمزاياها على الصواريخ الصلبة والسائلة ، مثل السلامة والود البيئي والتكلفة المنخفضة ، وعادة لا تحتوي على إضافات سامة. ومع ذلك ، فإن انخفاض معدل الانحدار وضعف كفاءة الاحتراق هي نقاط ضعف حرجة تؤثر على الأداء. لمعالجة هذه المشكلة ، تم إجراء تحقيقات مكثفة على الصاروخ الهجين المحترق النهائي المطعم بسبائك إنتروبيا عالية لتحسين معدل الانحدار وزيادة كفاءة الاحتراق. تم إجراء عمليات إطلاق ثابتة للحصول على الدفع ومعدل الانحدار والانديفاع المحدد. كما تم إجراء عمليات المحاكاة باستخدام برنامج لتقييم أداء سبائك الإنتروبيا العالية في محركات الصواريخ الهجينة. كانت السرعة المميزة ، والانديفاع المحدد ، ودرجة حرارة اللهب الأديباتية هي المعلمات الدافعة التي تم تحليلها. يركز التحقيق الحالي على صاروخ هجين مشتعل من طرف واحد يستخدم شمع البارافين المطعم بسبائك إنتروبيا عالية كوقود. أظهرت النتائج التجريبية أن إدراج سبائك الإنتروبيا المرتفعة بنسبة 5% ساهم في زيادة معدل الانحدار بنسبة 45.4% وزيادة 28.03% في الدفع و 25.89% زيادة في الانديفاع النوعي مقارنة بشمع البارافين النقي. أظهر الصاروخ الهجين المحترق النهائي أداءً أقل بشكل عام مقارنة بمحرك الصواريخ الهجين التقليدي بسبب الاحتراق غير المستقر في جميع أنحاء عمليات إطلاق النار. وفقًا للمحاكاة ، كلما زاد تركيز سبائك الإنتروبيا العالية ، كان أداءها أفضل بنسبة مؤكسد إلى وقود 1.3-1.0. يوفر الأكسجين الغازي كمؤكسد أفضل أداءً بشكل عام. ولكن بيروكسيد الهيدروجين يعمل بشكل أفضل في المؤكسد إلى الوقود أكبر من 4 توضح التجارب والمحاكاة إمكانات سبائك الإنتروبيا العالية لتعزيز معدل الانحدار ، والدفع ، والانديفاع المحدد لمحركات الصواريخ الهجينة. لم يظهر الحرق النهائي أيضًا أي تقلبات في ضغط المؤكسد إلى الوقود وضغط الغرفة أثناء الحالة المستقرة ، مما قد يكون مفيدًا في بعض التطبيقات. تسلط النتائج الضوء أيضًا على تأثير كتلة الوقود الأولية ، وتدفق الكتلة ، وسبائك الإنتروبيا العالية على أداء الصاروخ الهجين. يمكن لهذه التحسينات توسيع نطاق تطبيقات الصواريخ الهجينة والمساهمة في نمو أنشطة الفضاء التجارية والبحث العلمي وجهود استكشاف الفضاء.

# APPROVAL PAGE

I certify that I have supervised and read this study and that in my opinion, it conforms to acceptable standards of scholarly presentation and is fully adequate, in scope and quality, as a thesis for the degree of Master of Science in Engineering.



DR. MUHAMMAD HANAFI BIN AZAMI  
Assistant Professor  
Department of Mechanical Engineering,  
Kulliyah of Engineering,  
International Islamic University Malaysia,  
Kuala Lumpur 43600, Malaysia  
Tel : +603 8156 4472  
Email : hanafiazam@iium.edu.my

.....  
Muhammad Hanafi Azami  
Supervisor



DR NORHUDA HIDAYAH NORDIN  
Assistant Professor  
Department of Manufacturing and Materials Engineering,  
Kulliyah of Engineering,  
International Islamic University Malaysia,  
Kuala Lumpur 43600, Malaysia  
Tel : +603 8156 4472  
Email : norhuda@iium.edu.my

.....  
Norhuda Hidayah Nordin  
Co-Supervisor



DR. NUR AZAM BIN ABDULLAH  
Assistant Professor  
Department of Mechanical Engineering,  
Kulliyah of Engineering,  
International Islamic University Malaysia,  
Kuala Lumpur 43600, Malaysia  
Tel : +603 8156 4472  
Email : azam@iium.edu.my

.....  
Nur Azam Abdullah  
Co-Supervisor

.....  
Mohd Faisal Abdul Hamid  
Field Supervisor

I certify that I have read this study and that in my opinion it conforms to acceptable standards of scholarly presentation and is fully adequate, in scope and quality, as a thesis for the degree of Master of Science on Engineering.



Dr. Sher Afghan Khan  
Professor  
Department of Mechanical and Aerospace Engineering,  
Kulliyah of Engineering,  
International Islamic University Malaysia

.....  
Sher Afghan Khan  
Internal Examiner

.....  
Mohd Rashdan Saad  
External Examiner



This thesis was submitted to the Department of Mechanical and Aerospace Engineering and is accepted as a fulfilment of the requirement for the degree of Master of Science in Engineering.

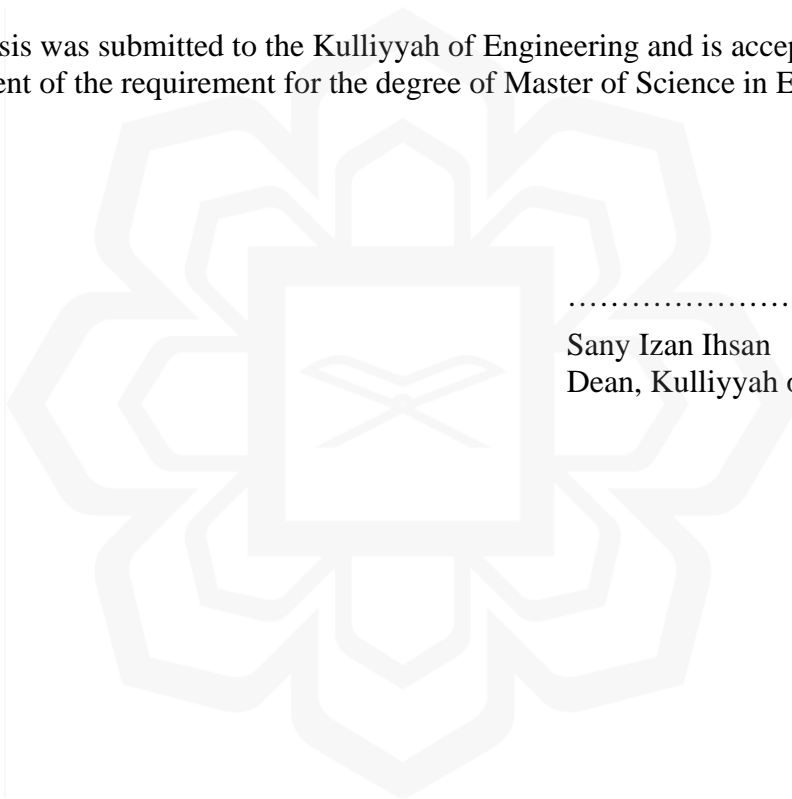
.....

Hanan Mokhtar  
Head, Department of Mechanical  
and Aerospace Engineering

This thesis was submitted to the Kulliyah of Engineering and is accepted as a fulfilment of the requirement for the degree of Master of Science in Engineering.

.....

Sany Izan Ihsan  
Dean, Kulliyah of Engineering



## DECLARATION

I hereby declare that this thesis is the result of my own investigations, except where otherwise stated. I also declare that it has not been previously or concurrently submitted as a whole for any other degrees at IIUM or other institutions.

Muhammad Ezamuddin Ezzad bin Sabri

Signature .....  .....

Date 31/10/2023



**INTERNATIONAL ISLAMIC UNIVERSITY MALAYSIA**

**DECLARATION OF COPYRIGHT AND AFFIRMATION OF  
FAIR USE OF UNPUBLISHED RESEARCH**

**INVESTIGATION OF END-BURNING TYPE HYBRID  
ROCKET MOTOR DOPED WITH HIGH ENTROPY ALLOY**

I declare that the copyright holder of this thesis are jointly owned by the student and IIUM.

Copyright © 2023 Muhammad Ezamuddin Ezzad bin Sabri and International Islamic University Malaysia. All rights reserved.

No part of this unpublished research may be reproduced, stored in a retrieval system, or transmitted, in any form or by any means, electronic, mechanical, photocopying, recording or otherwise without prior written permission of the copyright holder except as provided below

1. Any material contained in or derived from this unpublished research may only be used by others in their writing with due acknowledgement.
2. IIUM or its library will have the right to make and transmit copies (print or electronic) for institutional and academic purpose.
3. The IIUM library will have the right to make, store in a retrieval system and supply copies of this unpublished research if requested by other universities and research libraries.

By signing this form, I acknowledged that I have read and understand the IIUM Intellectual Property Right and Commercialization policy.

Affirmed by Muhammad Ezamuddin Ezzad bin Sabri



.....

Signature

31/10/2023

.....

Date

## ACKNOWLEDGEMENTS

In the Name of Allah, the Most Gracious, the Most Merciful. All praise is given to Allah for granting the power and abundance of benefits necessary to complete this report.

My supervisor, Asst. Prof. Dr. Muhammad Hanafi Azami, deserves special recognition for his patience, enthusiasm, insightful remarks, essential insights, helpful information, practical guidance, and never-ending ideas, all of which have greatly aided me in my study and preparation of this report. His extensive knowledge, profound experience, and professional expertise in Aerospace Propulsion, particularly hybrid rockets, as well as his invaluable assistance with constructive comments and suggestions throughout the progress of my Masters in Semester I 2022/2023 and Semester II 2022/2023, have all contributed to the success of this research.

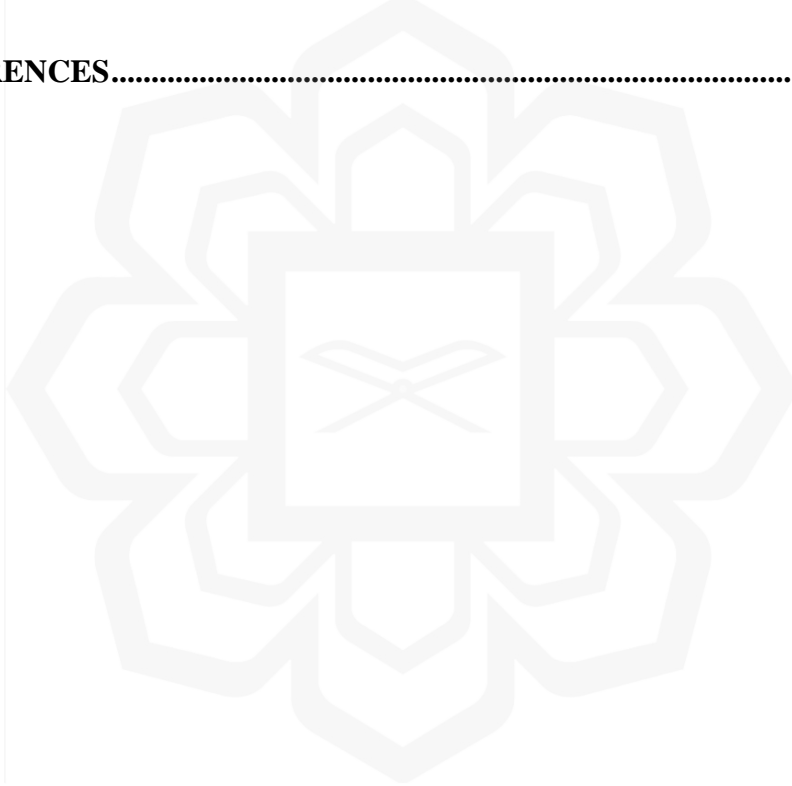
In addition, I am grateful to all lecturers in the Department of Mechanical Engineering for their generosity, hospitality, and technical support, as well as their permission to use the required equipment and materials after my project was completed. My heartfelt thanks to my loving parents, Sabri Mohd Arif and Rusna Md Zain, for their unending love, prayers, and encouraging words. I'd express my gratitude to all of my friends for their generosity and moral support throughout my studies. Your generosity means a lot to me, especially to those who contributed indirectly to my research. Thank you so much for everything.

Once more, we praise Allah for His unending generosity toward us, one of which has allowed us to successfully complete the composition of this thesis. Alhamdulillah.

# TABLE OF CONTENTS

Abstract .....	ii
Abstract in Arabic .....	iii
Approval Page.....	iv
Declaration.....	vi
Acknowledgements.....	viii
List of Tables .....	xi
List of Figures .....	xii
List of Symbols .....	xiv
<b>CHAPTER ONE: INTRODUCTION .....</b>	<b>1</b>
1.1 Overview .....	1
1.2 Research Significance .....	2
1.3 Problem Statement .....	2
1.4 Research Philosophy .....	3
1.5 Research Aim and Objectives .....	3
1.6 Research Methodology.....	4
1.7 Research Scope .....	4
1.8 Thesis Structure.....	5
<b>CHAPTER TWO: LITERATURE REVIEW.....</b>	<b>6</b>
2.1 Introduction .....	6
2.2 Interior Hybrid Motor Ballistics.....	8
2.3 Advantages of Hybrid Rocket.....	9
2.4 Disadvantages of Hybrid Rocket .....	10
2.5 Mitigation of the Drawbacks.....	12
2.7 End Burning .....	21
2.8 High Entropy Alloy.....	29
2.9.1 Definitions.....	29
2.9.2 Core Effects.....	30
2.9.3 Preparation of HEAs .....	32
2.9.4 Properties of HEAs .....	33
2.9.5 The Al-Co-Cr-Cu-Fe-Ni Alloy System.....	37
2.10 Concluding Remarks.....	39
<b>CHAPTER THREE: METHODOLOGY.....</b>	<b>40</b>
3.1 Introduction .....	40
3.2 Preliminary Design of an EBHR.....	41
3.3 Experimental Setup .....	44
3.3.1 Casing.....	44
3.3.2 Fuel.....	45
3.3.3 Feed System .....	48
3.3.4 Ignition System .....	50
3.3.5 Feed and End Caps.....	51
3.3.6 Nozzle .....	51
3.3.7 Data Acquisition System.....	52

3.3.8 Testbed .....	54
3.3.9 Test Setup.....	55
3.4 Data Reduction.....	56
3.5 Theoretical Performance Analysis of High Entropy Alloys .....	57
3.6 Concluding Remarks .....	59
<b>CHAPTER FOUR: RESULTS AND DISCUSSION .....</b>	<b>60</b>
4.1 Introduction .....	60
4.2 Firing Test Results .....	60
4.3 Fuel Regression Characteristic.....	66
4.4 Preliminary Design Analysis.....	67
4.5 Theoretical Analysis Results.....	68
4.6 Concluding Remarks .....	75
<b>CHAPTER FIVE: CONCLUSION AND RECOMMENDATIONS .....</b>	<b>76</b>
<b>REFERENCES.....</b>	<b>78</b>



## LIST OF TABLES

Table 2.1	Performance metrics with different number of ports	13
Table 2.2	Multiple-circular and wheel-typed eight ports design comparisons	14
Table 2.3	Regression rate data for metal additives used	16
Table 2.4	MHYCAS firing test results	25
Table 2.5	SuperMHYCAS test results	26
Table 2.6	ABS experimental results	26
Table 2.7	Fuel parameters (Miwa et al., 2020)	28
Table 2.8	Firing conditions and results (Miwa et al., 2020)	28
Table 3.1	Preliminary decisions for HRM design	42
Table 3.2	Rocket casing specifications	44
Table 3.3	PW fuel specifications	45
Table 3.4	HEAs composition	46
Table 3.5	HEAs with PW	46
Table 3.6	Nozzle specifications	52
Table 3.7	Testbed specifications	55
Table 3.8	Composition of FeCoNiAl(1-x)BxSi HEA powders	58
Table 3.9	Simulation conditions	59
Table 4.1	Test conditions	61
Table 4.2	Firing results	63
Table 4.3	Comparison of results between preliminary design and experiment	68
Table 4.4	Comparison of results between CEA-NASA and experiment	68
Table 4.5	Comparison of HEA1 and HEA2 with varying wt.% in paraffin wax	69

## LIST OF FIGURES

Figure 2.1	Schematic of a hybrid rocket	7
Figure 2.2	Illustration of a diffusion-controlled HRM combustion operation	8
Figure 2.3	Schematic diagram of swirling flow in a cylindrical grain	19
Figure 2.4	Comparison of results with and without mid injector	20
Figure 2.5	Axial-injection, end-burning hybrid	21
Figure 2.6	Flow field in the combustion chamber	23
Figure 2.7	Drawing of the MHYCAS engine	24
Figure 2.8	Drawing of the SuperMHYCAS engine	25
Figure 2.9	Visualisation chamber	27
Figure 2.10	Fabrication routes of HEAs	32
Figure 2.11	HEAs and conventional alloys' hardness comparison before and after annealing	34
Figure 2.12	Compressive behaviour of various HEAs	35
Figure 2.13	Comparison of $E_p$ and $I_{corr}$ between HEAs of $Al_xCoCrFeNi$ ( $x = 0.3, 0.5, \text{ and } 0.7$ ) and other conventional alloys in 3.5 wt% NaCl solution at room temperature	36
Figure 2.14	XRD patterns of $Pb_{1-x}SnTeSeLax$ HEAs	37
Figure 3.1	Research methodology flowchart	40
Figure 3.2	Preliminary design flowchart	41
Figure 3.3	PMMA casing	45
Figure 3.4	PW doped with HEAs	47
Figure 3.5	Fabrication process	47
Figure 3.6	Finished fuel	48
Figure 3.7	Feeding system diagram	48
Figure 3.8	Oxygen tank (left), pressure gauge and regulator (right)	49
Figure 3.9	Needle valve (left) and solenoid valve (right)	49
Figure 3.10	Feed line connection	49
Figure 3.11	Igniter controller	50
Figure 3.12	Igniter	51
Figure 3.13	Feed cap (left) and end cap (right)	51
Figure 3.14	Nozzle	52

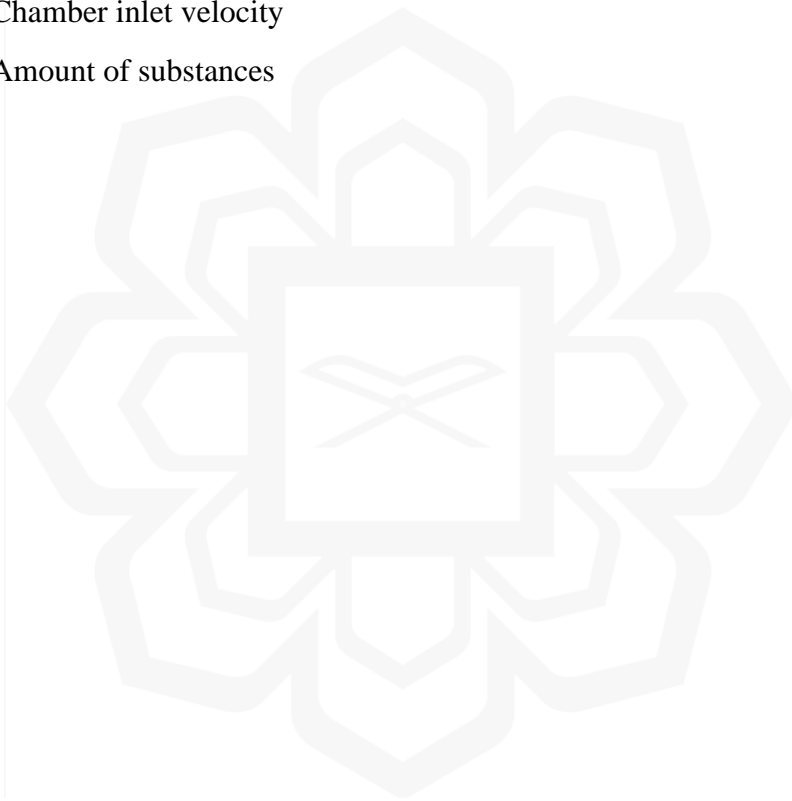


Figure 3.15	Data acquisition system	52
Figure 3.16	Thermocouple installation	53
Figure 3.17	Load cell	53
Figure 3.18	E10 pressure transmitter	54
Figure 3.19	Arduino UNO R3	54
Figure 3.20	Testbed	55
Figure 3.21	Experimental setup	56
Figure 3.22	Calculation flowchart for RT5	57
Figure 4.1	Firing sequence	62
Figure 4.2	Before (left) and after (right) combustion	62
Figure 4.3	Chamber pressure and temperature for each test	64
Figure 4.4	Regression rate and thrust for each test	64
Figure 4.5	Histories of chamber pressure and oxidiser mass flow rate (Test 2)	65
Figure 4.6	Histories of chamber pressure and O/F (Test 2)	65
Figure 4.7	Histories of chamber pressure and oxidiser mass flow rate (Test 6)	66
Figure 4.8	Histories of chamber pressure and O/F (Test 6)	66
Figure 4.9	The relationship between $\dot{r}$ and $P_c$	67
Figure 4.10	Comparison of results of CEA-NASA and experiment	69
Figure 4.11	Characteristic velocity of the concentrations of HEA2 as a function of O/F	70
Figure 4.12	Specific impulse of the concentrations of HEA2 as a function of O/F	71
Figure 4.13	Adiabatic flame temperature of the concentrations of HEA2 as a function of O/F	72
Figure 4.14	Characteristic velocity of the various oxidants as a function of O/F	73
Figure 4.15	Specific impulse of the various oxidants as a function of O/F	73
Figure 4.16	Adiabatic flame temperature of the various oxidants as a function of O/F	74
Figure 4.17	Comparison of characteristic velocity of various oxidants using CEA	75

## LIST OF SYMBOLS

$\alpha$	Regression rate coefficient
$A_f$	Fuel area
$A_p$	Port area
$A_t$	Nozzle throat area
$A_e$	Nozzle exit area
$C_p$	Specific heat
$c^*$	Characteristic exhaust velocity
$c_{ave}^*$	Time-averaged characteristic exhaust velocity
$c_{th}^*$	Theoretical characteristic exhaust velocity
$\varepsilon$	Nozzle expansion ratio
$F$	Thrust force
$\gamma$	Specific heat ratio
$G_f$	Fuel mass flux
$G_o$	Oxidiser mass flux
$g_o$	Gravitational constant
$I_{sp}$	Specific impulse
$K$	Thermal conductivity
$\lambda$	Nozzle efficiency
$L_p$	Port length
$M$	Molar mass
$M$	Mass
$M_e$	Exit mach number
$\dot{m}_f$	Fuel mass flow rate
$\dot{m}_o$	Oxidiser mass flow rate
$n$	Mass flux exponent
$\eta_c^*$	Characteristic exhaust velocity efficiency
O/F	Oxidiser-to-fuel ratio
$P_a$	Ambient pressure

$P_c$	Chamber pressure
$P_e$	Exit pressure
$\rho_f$	Fuel density
$\rho_o$	Oxidiser density
$\dot{r}$	Regression rate
$R$	Gas constant
$R_o$	Fuel grain outside radius
$T_f$	Flame temperature
$V$	Volume
$V_i$	Chamber inlet velocity
$X$	Amount of substances



# CHAPTER 1

## INTRODUCTION

### 1.1 OVERVIEW

Rocket propulsion can be classified based on the type of rocket engine and propellant employed. The three main categories are liquid, solid, and hybrid rockets. In a liquid rocket, the fuel and oxidiser are stored separately and combined in the combustion chamber. On the other hand, solid rocket propellants are pre-mixed and enclosed in a sturdy container.

This study specifically focuses on hybrid rocket motors (HRMs), which combine either a liquid or gaseous oxidiser with solid fuel. HRMs offer numerous advantages over traditional liquid or solid rocket propulsion systems, including enhanced safety, simplified fuel management, throttling capability, and environmental benefits. These factors have led to increased research and application of HRMs. Due to their ability to easily control the oxidiser mass flow rate, HRMs are well-suited for applications requiring variable thrust rockets in diverse scenarios.

However, conventional hybrid rockets have multiple disadvantages related to propulsion efficiency when compared with solid and liquid propellant rockets, which are low regression rate, combustion inefficiency, and fluctuating oxidiser-to-fuel ratio (O/F) throughout firing and throttling operations. End-burning combustion, where the combustion occurs at the end of the fuel surface, was reported to solve the O/F fluctuations problem. Using metallic additives have also proven to increase the performance of HRMs.

In this research, fuel doped with high entropy alloys (HEAs) and end-burning combustion are studied for their impact on the performance of the HRMs. HEAs are metallic additives that studies claimed to have better catalytic performance than conventional alloys due to their high surface area and vital adsorption energy. The context of the research significance, problem statement, research philosophy, research objectives, research methodology, research scope, and thesis structure are all discussed in this chapter.

## **1.2 RESEARCH SIGNIFICANCE**

There is currently a growing emphasis on enhancing propulsion safety, reducing costs, using environmentally friendly fuels and oxidisers, and achieving high functionality in propulsion systems. As a result, there has been an increased interest in hybrid propulsion systems. This interest is reflected in the involvement of various entities such as government agencies, large corporations, academic research institutions, and small enterprises in the research and development of hybrid rocket technology. These collective efforts have led to notable advancements in hybrid rocket propulsion, as documented by Chiaverini and Kuo (2007). In recent times, hybrid propulsion systems have gained significant attention as a viable option for launching satellites and other spacecraft.

The hybrid rocket propulsion system is being investigated in many areas of space transportation since it is relatively safe and has a higher capability for environmentally friendly technology compared to some other rocket propulsion technologies. On the other hand, the low regression rate is a significant drawback that prevents the widespread application of HRM. The limitations that continually occur in the hybrid propulsion system can be solved by conducting research and analytical investigation on the end-burning mode of the hybrid rocket, which is projected to increase the regression rate, and reduce O/F shift. The utilization of HEAs, which is reported to exhibit remarkable qualities such as improved mechanical and chemical properties, enhanced hardness, high fracture strength, yield stress, and plastic strain compared to conventional alloys, should also be investigated (Dada et al., 2019).

## **1.3 PROBLEM STATEMENT**

The lower regression rate of HRMs compared to solid and liquid rocket motors is one of the main problems. A low regression rate limits the rate at which the solid fuel grain is consumed, resulting in lower thrust levels and propulsion efficiency. The correlation between the regression rate and the combined mass flux of the fuel and oxidiser is directly proportional. Several variables, including the viscosity of the propellant, flame zone and the wall's enthalpy difference, blowing factor, fuel's density, solid fuel's vaporization, and gas' velocity at the boundary layer and down

the flame zone, affect the rate of fuel mass flux on the surface. Thermochemical characteristics primarily influence these parameters. The O/F shift in conventional HRM contributes to the combustion efficiency, influencing the regression rate.

Therefore, end-burning combustion will be used in this study as it is stated that there is no O/F shift in this mode. The thermochemical reaction of fuel can be altered by changing the fuel compositions. HEAs are viewed as a promising energetic metal additives compared to conventional alloys because of their high surface area and crucial adsorption energy. The nanosized HEAs catalyst is anticipated to boost regression rate and hence improve combustion efficiency of the propulsion system. The necessity for complex geometry to produce the necessary thrust will be eliminated by the significant increase in regression rate that is achieved. The focus of this study will be on the use of HEAs in HRM.

#### **1.4 RESEARCH PHILOSOPHY**

One of the innovative ideas for chemical rocket propulsion is the HRM. Due to its distinctive interior ballistic architecture, it stimulates in-depth propulsion studies. Although these investigations were conducted decades ago, most of them focused on improving the regression rate using vortex injectors, metal additives, fuel grain geometric modifications, and surface layer fuels that have been liquefied. There is, however, limited research on end-burning combustion and the effects of HEAs doping on liquefying fuels from the surface layer, such as paraffin wax (PW). Therefore, this research project aims to examine the functionality of a HEAs-doped end-burning lab-scaled HRM.

#### **1.5 RESEARCH AIM AND OBJECTIVES**

The aim of this project is to investigate the performance of the end-burning HRM using PW fuel doped with HEAs. To achieve this aim, the following objectives are highlighted:

1. To investigate the performance of end-burning HRM in terms of thrust, regression rate and specific impulse analytically.

2. To study the properties of HEAs as metallic additives in HRM in terms of characteristic velocity, specific impulse and adiabatic flame temperature.
3. To formulate and compare new empirical regression rate correlation utilizing the experimentally designed fuel.

## **1.6 RESEARCH METHODOLOGY**

Analytical analysis and experimental data provide the foundation of this study. Following is the research approach used:

1. Analytical calculations and preliminary design are developed. The design and analysis were based on previous works.
2. Fabricate PW fuel doped with HEAs.
3. Conduct static firing of HRMs in a lab-scaled testing facility.
4. Evaluate the experimental performance with the analytical calculations.

## **1.7 RESEARCH SCOPE**

The proposed hybrid rocket fuel doped with HEA and end-burning combustion might be able to increase the regression rate and boost combustion efficiency; however, this research is constrained by several restrictions. The HRM was studied at the lab scale with static firing because the primary goal of this research is to find ways to enhance the regression rate. For static firing, a sequence of circular port fuel is utilized. The essential parts are the feeding system, combustion chamber, nozzle, and data-collecting system. This research did not focus on the characterization of the mixture between HEAs and PW fuel.

The study did not consider the effects of aerodynamics or fuel structure for simplicity and early research. The equilibrium chemical reaction was thought to occur very slowly and be fully reacted in a frozen flow. In the analytical investigation, some parameters and ideal conditions were also assumed. The HRM's performance was assessed by evaluating the thrust, inlet and chamber pressure, and chamber temperature at various HEAs compositions.

## **1.8 THESIS STRUCTURE**

There are five chapters in this thesis. The overview of this research is briefly discussed in Chapter 1. Along with the problem statement, research significance, research objectives, research methodology, and research scope are also included.

A review of related literature is included in Chapter 2 to highlight and explain the parallels and differences between this research and earlier studies, particularly regarding the lab-scale end-burning hybrid rocket (EBHR) design and additives used.

The preliminary design and the analytical approach used to analyze the performance of HRMs are covered in Chapter 3. Additionally, this chapter has the explanation on the design and construction of a lab-scale HRM. The lab-scale HRM's parts are exhaustively detailed.

The outcomes of the analytical and experimental work are thoroughly analyzed and evaluated in Chapter 4. This chapter explored the evaluation and analysis of the HRMs' performance using different design characteristics. The results were compared to demonstrate the dependability and precision of the analytical computations.

The research projects discussed in the earlier chapters are summed up and concluded in Chapter 5. Additionally, recommendations and potential future projects are also included.



## **CHAPTER 2**

### **LITERATURE REVIEW**

#### **2.1 INTRODUCTION**

The goal of improvements in rocket propulsion is always to achieve higher performance, improved dependability, and lower production costs. Hybrid rocket technologies will be the main topic of this literature review. The regression rate is a metric used in assessing the HRM's performance. The rate of fuel surface regression during a burn is known as the regression rate; the higher the regression rate, the better the performance. Conducting the combustion in end-burning mode is one of many investigations and tests to improve the rockets' regression rate. For end-burning, the combustion occurs at the fuel end towards the rear of the chamber. This literature review will concentrate on the end-burning mode's potential in hybrid rocket propulsion.

Comprehension of the rocket systems' structure, internal ballistic, theoretical knowledge, and prior research is needed to understand the significance of end burning on the regression rate in an HRM. The relevant background information on rocket propulsion is explained in this literature study for a better understanding of the HRM. The classifications and descriptions of various rocket systems will be covered in this chapter, focusing on the hybrid rocket, which will be the subject of the entire study. The development of the rocket system from its inception to the established and current initiatives of the twenty-first century is depicted in the history of the hybrid rocket system, which will also be covered. A hybrid rocket's benefits, drawbacks, and mitigations to each issue are covered in detail. The two chapters' final section will discuss the concept of end burning, its effect on the HRM, and high entropy alloy.

HRM uses liquid and solid propellants, which are kept in separate tanks. In addition to the traditional design, hybrid propellant systems can come in mixed hybrid or tribrid configurations. The most typical arrangement, known as the "classical configuration," uses solid fuel in conjunction with a liquid or gaseous oxidiser. Inverse hybrid vehicles run on liquid fuel and solid oxidisers. Because solid oxidiser is challenging to manufacture, it is not as feasible as the preceding version.

In a tribrid configuration, a mixture of solid oxidiser combined with solid fuel undergoes combustion with a separate liquid oxidiser. The various configurations were created to increase the regression rate, a critical problem with hybrid rockets. The fuel regression rate determines the total mass flow rate and total oxidiser-to-fuel mixture ratio, which regulate the specific impulse and thrust for a specific chamber pressure.

The essential parts of an HRM are depicted in Figure 2.1. The oxidiser is delivered to the combustion chamber by a single fluid feed system managed by the main run valve. The liquid oxidiser typically converts into gas when it enters the chamber, and when the gas oxidiser travels over the solid fuel, it heats it. The solid fuel will pyrolyze into gas fuel at that point. As a result of the reaction involving the fuel and oxidiser in proximity to the solid fuel surface, a turbulent and reactive boundary layer is formed. The combustion process in the chamber of the hybrid rocket follows standard diffusion combustion principles. The most crucial element in measuring the effectiveness of the HRM is the regression rate, which represents the rate of solid fuel pyrolysis. It depends on the circumstances surrounding gasification and the amount of thermal energy used during gasification (Zhao et al., 2018).

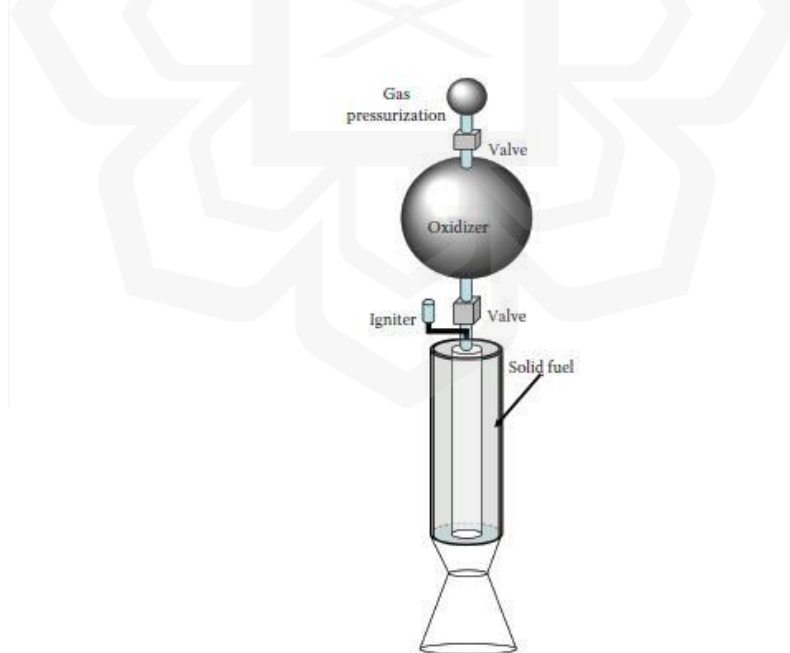


Figure 2.1 Schematic of a hybrid rocket (Travis, 2017)

## 2.2 INTERIOR HYBRID MOTOR BALLISTICS

The conventional hybrid configuration, where there is no oxidiser present in the fuel grain, leads to combustion occurring only in the gaseous phase. This causes notable differences in fuel surface regression rates compared to solid rocket engines. Sutton and Biblarz (2017) stated that the regression rate of the fuel surface is closely connected to the fluid dynamics of the combustion port and the transfer of heat to the surface of the fuel. The solid fuel needs to evaporate before combustion can take place.

The formation and expansion of a boundary layer over the fuel grain surface is believed to contain the primary combustion region. The surfaces of the fuel grain receive heat through radiation and convection. The specific characteristics of a hybrid motor are heavily dependent on the propellant used, as well as the size and arrangement of the combustion chamber, which are typically determined through empirical research. Figure 2.2 provides an illustration of the HRM combustion operation for a non-metallized fuel system (Sutton & Biblarz, 2017).

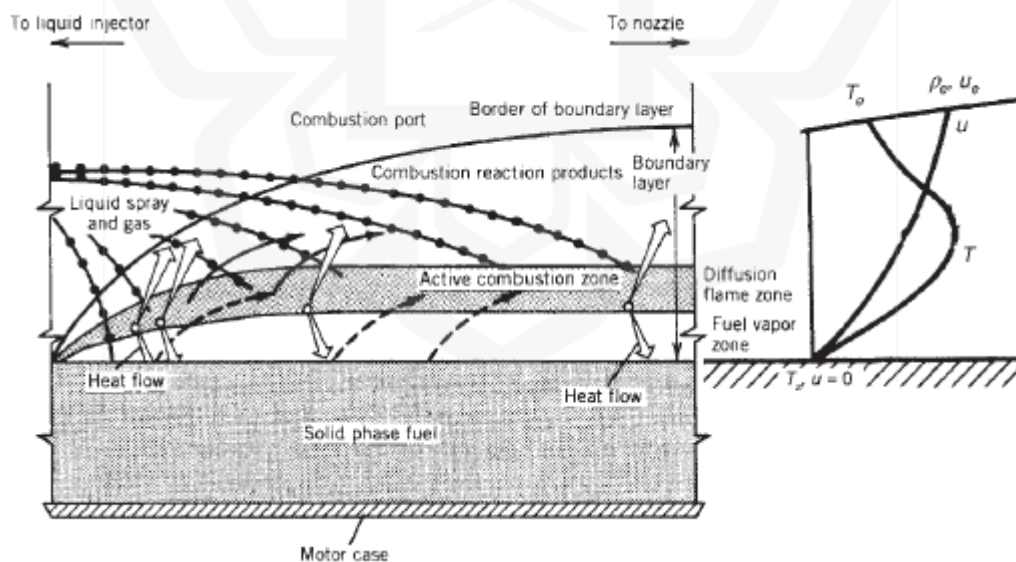


Figure 2.2 Illustration of a diffusion-controlled HRM combustion operation (Sutton & Biblarz, 2017)

According to Sutton and Biblarz (2017), fuel that has evaporated due to the heating of the flame zone flows away from the surface and into the flame region while

oxidiser convects by turbulent diffusion from the free stream to the flame zone. The boundary layer location where the flame first appears is solely dictated by the stoichiometry necessary for combustion. The rate of oxidation reactions plays a significant role in determining how thick this flame zone is. These rates often follow an exponential relationship with temperature and are heavily influenced by local pressures.

In addition to pressure and gas temperature, other variables that influence the formation of the fuel-grain boundary layer and, consequently, the features of fuel regression include grain design, oxidiser mass flow rate, port length, and cross-sectional area. Convection is thought to transfer heat much more effectively than gas-phase radiation or radiation from soot particles in the flow with non-metallised fuel grains. As a result, investigations of convective heat transfer in a turbulent boundary layer can be used to investigate the fundamental properties of fuel grain regression. For the fuel regression rate,  $\dot{r}$ , the following equation may be used:

$$\dot{r} = a(G_o)^n \quad (1)$$

$G_o$  is the oxidiser mass velocity, which is calculated by dividing the oxidiser mass flow rate by the cross-sectional area of the combustion port. Additionally, the constants  $a$  and  $n$  are determined via empirical fitting. This equation suggested that HRM's fuel regression rates are strongly dependent on  $G_o$ .

### **2.3 ADVANTAGES OF HYBRID ROCKET**

HRMs offer distinct advantages over both liquid and solid-fueled rockets, with a combination of evident and subtle benefits. One of the primary advantages of HRMs is their safety. HRMs typically utilize inert solid fuel grains, and their burn rate is determined by the mass flux rate of the oxidizer. This design makes the propellant grain more forgiving of manufacturing flaws, such as cracks, reducing the risk of catastrophic failures. Moreover, since the fuel and oxidizer are stored separately until combustion, HRMs have fewer potential failure modes.

Consequently, the risk of explosions is greatly diminished. Handling precautions are also less stringent compared to solid-propellant rockets, which require extensive inspections due to the non-explosive nature of propellants during the mixing phase in the combustion chamber. Additionally, the propellant grain is highly resistant

to auto-ignition from heat and impervious to ignition from stray electrical charges (Altman, 1991; Pastrone, 2012).

Hybrid rockets offer a wider range of propellant options compared to liquid or solid rockets. The ability to combine various fuel mixtures and additives for regression rate enhancement provides researchers with ample flexibility for propellant development. Ongoing investigations into optimal hybrid rocket fuels involve experimenting with a variety of additives and fuel mixtures, further expanding the range of potential propellants (Chiaverini & Kuo, 2007).

Simplicity in design and operation is another notable advantage of HRMs. They require fewer plumbing components, fewer valves, and simpler control systems due to their reduced need for complex feeding systems. This streamlined approach results in easier handling and fewer potential failure points. The non-explosive nature of hybrid rocket propellants allows for less rigorous handling precautions compared to solid-propellant rockets, which demand extensive and comprehensive inspections at each preparation stage (Gharat & Hastak, 2022).

HRMs possess the unique capability of throttle control, which sets them apart from solid rocket engines. This feature enables precise control of thrust levels and the ability to stop and restart the rocket engine, enhancing manoeuvrability and versatility in mission profiles (Jens et al., 2016).

In summary, hybrid rocket technology presents a range of advantages, from enhanced safety and propellant versatility to simpler designs and throttle capabilities. These characteristics make HRMs an appealing choice for various aerospace applications, offering unique benefits for both scientific research and commercial space ventures.

## **2.4 DISADVANTAGES OF HYBRID ROCKET**

When comparing hybrid rockets to liquid and solid rockets, several additional drawbacks become apparent. Conventional HRMs often face limited adoption, particularly in high-thrust applications, primarily due to their suboptimal fuel regression rates. The use of polymeric fuels like HTPB or HDPE is a contributing factor to these low regression rates. To compensate for these slow regression rates, multi-port fuel grains are commonly employed to provide higher mass flow rates

(Kobald et al., 2017). However, these multi-port grains often exhibit structural deficiencies and subpar volumetric efficiency.

As reported by Whitmore (2015), the fuel regression rates of hybrid rockets tend to be around 25% lower than those of solid propellant motors in a similar thrust range. This reduction in regression rates can lead to undesirable consequences, such as elevated O/F, reduced motor duty cycles, nozzle erosion, and motor instability. Various strategies, including increasing the number of fuel ports, introducing fuel component liquefaction, and metallizing the grain, have been explored to address this regression rate challenge. However, each strategy presents its own set of developmental hurdles.

In many hybrid rocket systems, the O/F ratio experiences fluctuations over time due to fuel port diameter expansion during combustion and variations in oxidizer flow rates, particularly in throttling scenarios (Karabeyoglu & Evans, 2014). This phenomenon negatively impacts motor performance and can lead to off-peak operation from a chemical performance perspective. Notably, well-designed hybrid rockets exhibit minimal sensitivity to O/F shifts at their peak performance levels. For systems with deep throttling requirements, aft oxidizer injection has been considered as a viable solution to maintain overall efficiency.

Inefficient combustion resulting from inadequate mixing of unreacted fuel and oxidizer within the mixing chamber is another challenge faced by hybrid rockets. Large diffusion flames inherently lead to incomplete mixing of fuel and oxidizer at the grain port outlet, ultimately causing a decline in specific impulse. HRMs generally exhibit combustion efficiencies 1-2% lower than solid and liquid rocket engines (Pastrone, 2012). Conventional HRMs featuring multiple ports may encounter difficulties in achieving complete fuel combustion, as portions of the fuel between the ports can detach from the main grain and obstruct the nozzle (Chiaverini & Kuo, 2007). Consequently, a small percentage of the fuel may remain unburned following motor burnout. The impact of this unburned fraction, known as the sliver fraction, on rocket performance is evident, as it necessitates a higher fuel consumption to generate equivalent thrust, particularly in circular port configurations (Sutton & Biblarz, 2017).

In summary, while hybrid rockets offer several advantages, they also face notable challenges related to fuel regression rates, O/F ratio shifts, and combustion inefficiencies. Addressing these issues is crucial to harnessing the full potential of hybrid rocket technology in various aerospace applications.

## 2.5 MITIGATION OF THE DRAWBACKS

Some structural and chemical changes to the fuel grains have already been made to attain adequate regression rates. Some modifications include complex port geometries to ensure swirling flow with a rotational component in the flow vector, multiple ports to increase surface area or the addition of specific chemicals to the fuel to increase heat transfer.






### 1. Multiple Ports

One method for raising the regression rate in HRMs involves using multiple ports. As a result, the desired chamber pressure can be obtained due to an increase in the effective burning surface area. However, the complicated manufacturing process is the fundamental difficulty in multi-port grain design. According to the numerical simulation done by Tian et al. (2014), the flow fields and fuel regression rates of the multi-port HRM have three-dimensional characteristics. As the axial location increases, the fuel regression rates first decrease and then gradually rise.

For a particular cross-section, the location of the flame and the fuel port profile is related to the distribution of the fuel regression rate. The fuel regression rates are lower in specific locations on arcs with smaller radiuses of curvature when the fuel port is a derivable convex figure. As the number of ports expanded due to the improvement in regression rate, experimental data revealed that the O/F ratio fell while the oxidiser mass flow rate was maintained. In the 14-port scenario, the length was also decreased, sometimes by as much as 70%. Additionally, the volumetric and characteristic velocity efficiency increased (Ahn et al., 2018).

The findings done by Azami (2014) demonstrate that having several ports in a fuel grain is advantageous for boosting the regression rate. The turbulent flow in the chamber downstream, the degree of flow mixing and the utilization of multiple combustion ports causes the increase of combustion efficiency in HRMs (Sutton & Biblarz, 2017). It demonstrated that the regression rate has improved for several port designs. However, this necessitates an expansion in the grain diameter design. An increase in chamber diameter correlates with an increase in regression rate. Table 2.1 shows the performance of multi-port HRMs.

Table 2.1 Performance metrics with different number of ports (Azami, 2014)

No of Ports	6	7	8	9	10
Performance Parameter					
Fuel length (m)	1.83	1.66	1.51	1.38	1.26
Web (cm)	6.85	6.77	6.73	6.71	6.7
Fuel volume per port (m <sup>3</sup> )	0.064	0.055	0.048	0.043	0.039
Final area of port (m <sup>2</sup> )	0.04	0.037	0.035	0.034	0.033
Final perimeter of port (m)	0.71	0.68	0.67	0.65	0.64
Final surface area of port (m <sup>2</sup> )	1.29	1.13	1.00	0.91	0.82
Radius of center hole (cm)	6.8	8.8	10.9	12.9	15
Radius of grain (m)	0.29	0.31	0.33	0.35	0.37
Regression rate (mm/s)	2.08	2.11	2.14	2.17	2.19

## 2. Geometric Modifications

The hybrid rocket's regression rate was further enhanced by considering helical port designs. According to Whitmore et al. (2015), considerable increases in fuel regression rates were found when helical fuel ports were compared to cylindrical fuel ports. As the helical fuel port burned to become more cylindrical, these gains in regression rate started to decline over time. Mean regression rate amplification factors as a function of oxidiser mass flux are greater than 4 for the most aggressive helical port geometries with low pitch lengths. The average amplification factors of even the tiniest helical ports were discovered to be greater than 2. Calculations show that around 75% of the regression rate amplification is accounted for by increases in skin friction brought on by helical rotation. The remaining amplification results from centrifugal flow's suppression of radial wall blowing (Whitmore & Walker, 2017).

Zhang (2016) investigated how star swirl grain port affected the regression rate. According to the results, the star swirl grain's burning



surface area grew by nearly 200% and its spatially averaged regression rate by about 60% compared to the tube grain under the same port area and grain length. The enormous vortex around the axis in the aft mixing chamber allows the oxidiser to burn properly. The performance of the hybrid motor is more outstanding and more reliable with star swirl grain (Paccagnella et al., 2017). In HRM firing tests with a swirl injector, Sun et al. (2016) found an increase of 200% in the average regression rate as the swirl amount grows. Still, because swirl strength weakens as the axial distance grows, the increased regression rate is focused mainly on the area around the fuel port entry.

Table 2.2 from Azami (2014) demonstrates that wheel-shaped ports need a larger fuel grain but a shorter length for the wanted thrust. Wheel-shaped ports with thicker webs benefit from longer burning times. Additionally, wheel-shaped ports have a larger combustion surface area with a minimum increase of 30%. From the findings, the mean regression rate has increased by 5%. The findings corroborated this since, for short fuel grains, the boundary layer does not fully form along the longitudinal port axis. In contrast, the full oxidiser supply is used up for long fuel grains before the grain is finished. Without it, the downstream portions of the fuel grain will fruitlessly vaporize. (Kuznetsov & Natan, 2003).

Table 2.2 Multiple-circular and wheel-typed eight ports design comparisons (Azami, 2014)

	Multiple-Circular Ports	Wheel-Typed Ports
Grain Diameter (m)	0.6	0.66
Fuel Length (m)	2.07	1.51
Web thickness (m)	0.06	0.07
Final area of each ports (m <sup>2</sup> )	0.03	0.04
Final surface area of each ports (m <sup>2</sup> )	1.19	1.00
Average regression rate (cm/s)	0.20	0.21

### 3. Energetic Fuel Additives

The energetic additives' chemical properties can be used to solve the low regression rate problem. This technique increases the regression rate by incorporating high-energy fuel elements like metal and metal hydrides into the solid fuel grain. The advantage of metal powder is that it reduces the heat at which fuel vaporises. One way to reduce the non-uniformity of the local fuel regression rate is to increase the concentration of non-homogeneous fuel additives. Unburned fuel is the cause of the test motor's head and aft caps having slivers. During combustion, this will lead to early port merging in the pre and aft-section, which causes instability during operation.

According to Sun et al. (2016), Risha and Evans investigated how energetic fuel addition affected the behaviour of regression rate in HRMs of different sizes and found that Al<sub>2</sub>O<sub>3</sub> aluminium particles boosted the mass burning rate by around 42% compared to pure HTPB. Risha and Evans also used several firing experiments to examine how aluminium affected the pace of regression. They found that metal with nanometer-sized particles has the most significant impact on the regression rate, with an addition of 20% aluminium raising the regression rate by 40%. Test results showed that the increased regression rate of paraffin fuel used in HRMs, which Karabeyoglu discovered and investigated, is almost three times higher than that of HTPB fuel (Sun et al., 2016). However, they found that the paraffin burns less effectively. These paraffin-based fuels have a three to five times higher regression rate at comparable mass flows than polymers.

Carrick and Larson investigated cryogenic solid hybrid rocket fuels, another fuel mixture. Using cryogenic solid n-pentane, they measured regression rates 5–10 times higher than those of polymeric hybrid fuels (Kobald et al., 2017). These propellants often exhibit regression rates that rely on pressure and mass flux. This strategy works well, but its main drawback is the complexity in manufacturing, handling, and shipping expenses brought on by a higher hazard classification. A comparison of various metal additives used in hybrid rocket designs from earlier studies by Yash Pal et al. (2021) are shown in Table 2.3.

Table 2.3 Regression rate data for metal additives used (Pal et al., 2021)

Fuel	Oxidiser	Additives	Oxidiser Mass Flux [kg/m <sup>2</sup> s]	Regression Rate [mm/s]	Findings
Hydroxyl-terminated polybutadiene	O <sub>2</sub>	Activated Aluminium	120–220	0.9–1.6	Inclusion of activated aluminium in HTPB resulted in a 40% improvement in regression rate as opposed to pure HTPB. The physical ablation of high-molecular-weight particles from the fuel surface played a role in controlling the entire regression procedure.
Hydroxyl-terminated polybutadiene	O <sub>2</sub>	Ammonium perchlorate, Aluminium	40–450	0.6–2.6	Under high mass flux conditions, AP/Al greatly enhanced the regression rates by providing an extra heat source close to the fuel surface.
Hydroxyl-terminated polybutadiene	O <sub>2</sub>	Aluminium, Boron	70–180	0.82–2.4	Viton-A coated Alex® loaded fuel mix showed an almost 120% improvement in regression rate, while B-based additives showed a minimum of 68% increase in regression rates.
Hydroxyl-terminated polybutadiene, Paraffin	O <sub>2</sub>	Tungsten, Silberline Aluminium flakes	100–150	0.9–1.5 (4–7)	Nano-tungsten powder enhanced the fuel regression rate of HTPB by 38%. Solid fuels based on paraffin and loaded with Silberline® aluminium flakes exhibited about a 30% increase in linear regression rates.
Dicyclopentadiene	H <sub>2</sub> O <sub>2</sub>	Lithium aluminium hydride	143–263	1.3–1.42 (1.64–2.37)	DCPD showed only a marginal gain over HTPB, and LiAlH <sub>4</sub> inclusion led to increased rates of regression.
Polytetrafluoroethylene, Hydroxyl-terminated polybutadiene	O <sub>2</sub>	Boron	89–218	0.53–0.66	A regression rate correlation ( $rb[\text{cm/s}] = 0.042(P[\text{MPa}])^{0.531}$ ) was obtained, and the measurement of solid regression rates was unattainable because of surface char development.
Hydroxyl-terminated polybutadiene	O <sub>2</sub>	Aluminium	244–378	0.665–1.010	HTPB and Al mixed fuel coated with fluorel-plus-ester (VF-ALEX series) presented remarkable regression rates at every oxidiser mass fluxes.

Dicyclopentadiene, Hydroxyl-terminated polybutadiene	H <sub>2</sub> O <sub>2</sub>	Sodium borohydride, Aluminium hydride	281–478	1.25–1.6 (1.5–2.0)	47% more regression rate was seen with addition of 50 wt.% NaBH <sub>4</sub> fuel compared to pure DCPD. AlH <sub>3</sub> in DCPD increased the neat DCPD regression rate approximately 85% at high mass flux levels.
Polyurethane foam, Paraffin	O <sub>2</sub>	Lithium aluminium hydride, Magnesium hydride, Aluminium	100–350	~0.4–2.5	When compared to pure HTPB, the introduction of LiAlH <sub>4</sub> increased HTPB's regression rate by as much as 378%. The regression rate was boosted around five times higher by wax-based fuel that had been added MgH <sub>2</sub> and Al than by HTPB.
Hydroxyl-terminated polybutadiene	O <sub>2</sub>	Magnesium hydride, Aluminium, Magnesium, Iron	90–400	0.56–4.54	Mg and Fe loaded fuels reported an increase in regression rate by 50%. Uncoated Al mixed with HTPB exhibited low-frequency pressure oscillations of large amplitude, while Mg and MgH <sub>2</sub> loaded fuels shows steady operation.
Hydroxyl-terminated polybutadiene	O <sub>2</sub>	Aluminium	90–325	0.5–1.8	55% and up to 140% improvement in regression rate was shown with 10% Al compared to pure HTPB and mechanically activated Al in polytetrafluoroethylene, respectively.
Paraffin, Polyethylene	O <sub>2</sub>	Aluminium	42-110	0.7-2.4	Addition of 5-25% Al increases the regression rate by 95%.
Hydroxyl-terminated polybutadiene, Polyethylene, Paraffin	O <sub>2</sub>	Oleamide, Polydextrose, PEG6000, Magnesium	75–350	0.18–0.58 (0.8–3.7)	The incorporation of PE/oleamide enhanced the regression rates by up to 21%. MgP-doped self-disintegrating fuels showed a significant increase of 163.2% in regression rates.
Hydroxyl-terminated polybutadiene, Paraffin	O <sub>2</sub>	Lithium aluminium hydride, Magnesium hydride	35 to 130	0.5–3.5	The formulations loaded with MgH <sub>2</sub> displayed the highest enhancements, reaching up to 353% in comparison to the base fuel and HTPB.

#### 4. Entrainment

According to Chiaverini & Kuo (2007), Stanford University proposed that fuels forming low-viscosity melt layers could entrain liquid droplets due to the gas flow's shear stress in the port. High gas flux, low-viscosity melt layers can lead to liquid layer instability, resulting in the discharge of liquid droplets. Cryogenic compounds and certain non-polymerizable fuels, like alkanes, exhibit this phenomenon. Liquid entrainment can significantly impact the regression rate due to two factors:

1. Liquid droplets formation requires less heat (heat of fusion) compared to vaporization (heat of vaporization).
2. Reduced gas flow from the surface (blowing) leads to decreased convective heat transfer blockage.

With entrainment, the blowing term (B) is less than 2, indicating reduced heat-transfer blockage, whereas conventional polymeric hybrid fuels have a B value between 5 to 20, resulting in significantly higher heat-transfer blockage (Chiaverini & Kuo, 2007). Porous wall cooling benefits from this effect in combustion chambers. High alkanes, including various paraffins, can exhibit liquid layer characteristics suitable for droplet entrainment. ORBITEC also achieved similar results when studying solid  $O_2$ ,  $CH_4$ ,  $C_2H_2$ , and  $H_2$ , with solid  $H_2$  showing nearly 20 times higher regression rates than HTPB.

To address droplet residence time for complete combustion, an aft combustion chamber, approximately 1/2 the diameter in length to enhance mixing, was added (Chiaverini & Kuo, 2007). The Space Propulsion Group and Stanford University adapted a paraffin-based fuel to meet the viscosity and surface tension requirements for liquid entrainment. Lab tests initially demonstrated enhanced burning rates using pentane and GOX. Scaled-up tests, supported by NASA and DARPA, showed regression rate increases of 200 to 300% for various oxidizers and a single-port, paraffin-based fuel. These findings suggest that simple one or two-port grain designs can be used in larger motors in the 100–1000 kN range (Chiaverini & Kuo, 2007).

## 5. Oxidiser Flow

A systematic approach for raising regression rates in HRMs using solid fuels is integrating swirling flows, which essentially provide an extra tangential flow. An ORBITEC experiment employed a forward-and-aft injection, reversing the vortex-flow approach. Compared to the typical axial-flow configuration, the fuel regression rate rose by up to eight times (Wongyai & Greatrix, 2016). The swirl injector propels the oxidiser into the combustion chamber at a high tangential velocity to increase the wall heat flow and the mixing of the combustion reactants, which in turn increases the regression rate and combustion efficiency. Figure 2.3 shows the motion of the oxidiser flow in the motor.

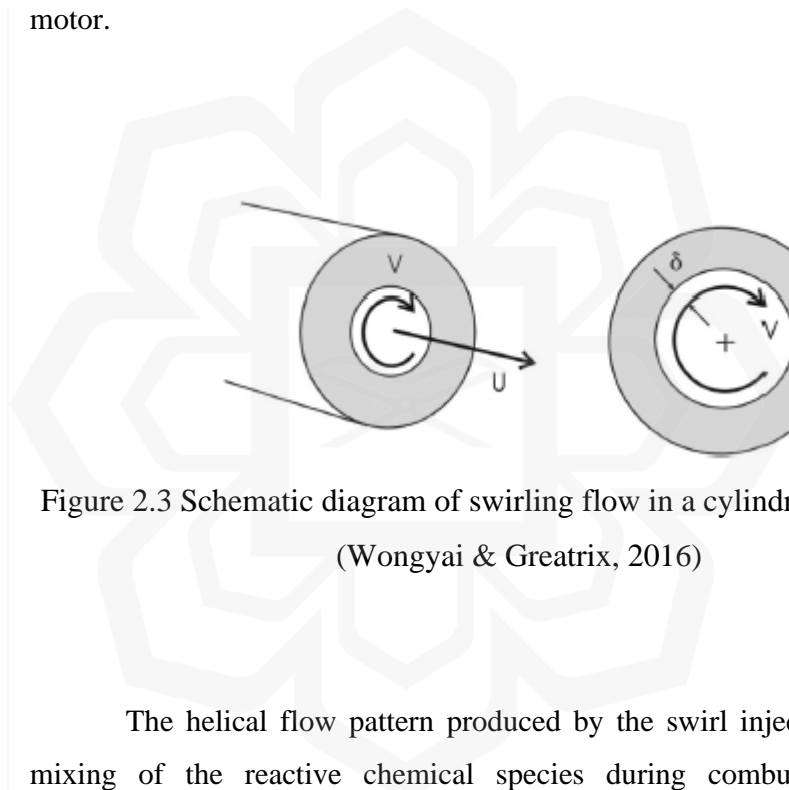


Figure 2.3 Schematic diagram of swirling flow in a cylindrical-grain HRM (Wongyai & Greatrix, 2016)

The helical flow pattern produced by the swirl injector enhances the mixing of the reactive chemical species during combustion and raises combustion efficiency. This flow type increases the regression rate by raising the oxidiser mass's wall heat flux and effective velocity flowing onto the solid fuel grain (Pal et al., 2021). The regression rate and performance of the hybrid motor improve with increasing injection swirl number and oxidiser mass flux (Paccagnella et al., 2017).

## 6. Turbulence Generators

Developing designs that generate a lot of turbulence at the burning surface and increase the heat-transfer coefficient has been another well-liked tactic. According to Vignesh & Kumar (2020), the mid injector causes turbulence

when oxygen is not being given, which causes the rate of regression to accelerate. If only the head-end swirl injector is used, incorporating a turbulent generator in the combustion chamber can lead to an enhanced regression rate. Therefore, combining a turbulence generator and swirl injector in the combustion chamber will result in a greater regression rate.

The swirling flow of oxidiser from the mid-injector, which has a larger diameter port (35 mm) compared to the fuel grain port of the second combustor (15 mm), impinges on the fuel surface of the subsequent combustor, thereby improving the regression rate. This is one of the reasons for achieving a higher regression rate when a cavity or mid-injector is present without an oxygen supply. Moreover, the increased mass flux from the improved regression rate in the first combustor transfers mass to the following combustor. This results in a higher heat feedback to the surface of the fuel and a larger regression rate in the second combustor, both attributed to the increased mass flux. Consequently, an overall higher regression rate is observed (Vignesh & Kumar, 2020). Figure 2.4 compares the regression rate with and without the mid-injector.

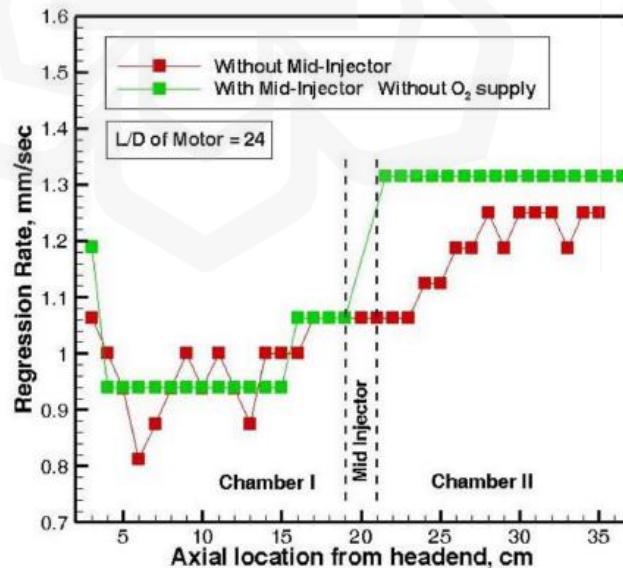


Figure 2.4 Comparison of results with and without mid injector (Vignesh & Kumar, 2020)

## 2.7 END BURNING

Throughout the operation of a classical HRM, a combustion flame forms on the fuel side surface when the oxidiser is sprayed into the solid fuel port. This process is accompanied by a shift in the O/F ratio during throttling and firing. This O/F shift leads to a decrease in specific impulse and a probable increase in unused propellant weight (Saito et al., 2019). During firing, the O/F will likely rise as the fuel port becomes wider and the regression rate drops. (Karabeyoglu & Evans, 2014). On the other hand, for end-burning hybrid rockets (EBHRs), combustion starts at the rear of the fuel; as a result, the combustion surface area and propellant mass flow rate are constant (Pal et al., 2021).

The regression rates of axial injection and EBHRs have been found to be primarily influenced by chamber pressure rather than the oxidiser mass flow, resulting in minimal variations in the mixture ratio during operation (Hitt & Frederick, 2017). A crucial element of the EBHR design is the utilization of a cylindrical fuel grain with multiple small ports arranged in the axial direction for the passage of oxidiser gas. The operation of the EBHR is illustrated in Figure 2.5.

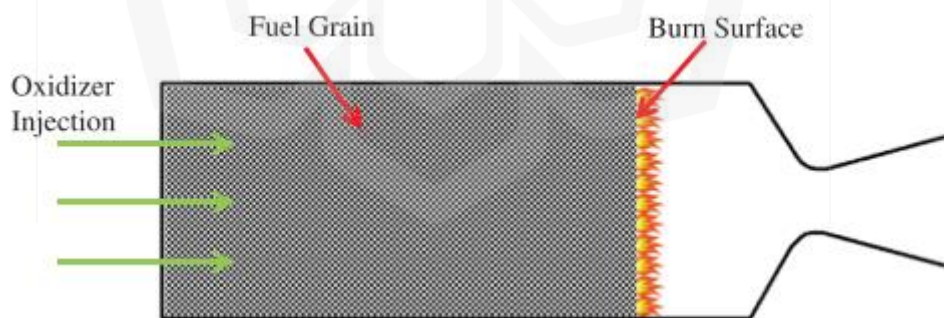


Figure 2.5 Axial-injection, end-burning hybrid (Hitt & Frederick, 2017)

To create end-burning combustion, it is crucial to stop a flame from growing upstream in a port and to maintain the envelope flame at the exit surface. For this purpose, a straightforward analysis using a single port fuel indicated that a fuel must have a volumetric filling rate greater than 0.953 (Nagata et al., 2017). The



manufacture of complicated solid fuel geometries with the accuracy needed to realise the EBHR concept is now possible thanks to recent advances in three-dimensional (3D) printing technology.

A paper by Nagata et al. (2017) describes an innovative type of end-burning hybrid rocket that has become achievable due to recent advancements in three-dimensional printing technology. The results of verification firing tests are presented, showing that the O/F ratio remains constant during firing and clearly distinguishing between the initial transient and stable periods of the end burning mode. By achieving an initial end-face form that closely resembles the steady-state shape, the duration of this initial transient period can be shortened since it represents the time required for the exit end-face to reach a steady-state shape.

According to Saito et al. (2019), three criteria were established for an effective EBHR: An ideal O/F that can be achieved by having a high starting fuel area fraction, tiny port intervals that shorten the duration of a port amalgamation, and ports distributed throughout the whole fuel section. They studied the fuel regression characteristics of axial-injection EBHRs under relatively high-pressure conditions. Gaseous oxygen was used as the oxidiser during firing tests performed at chamber pressures and oxidiser port velocities ranging from 0.22 to 1.05 MPa and 31 to 103 ms, respectively. Fifteen static firing experiments yielded findings that demonstrated a roughly linear increase in the fuel regression rate with chamber pressure. The regression rates varied from about 1.1 mm at 0.25 MPa to 5.4 mm at 0.71 MPa.

Additionally, it was shown that the oxidiser port velocity did not affect the fuel regression rates. They discovered an issue called backfiring and investigated the problem analytically using a computation model, which was then utilised to demonstrate that the problem was effectively prevented by enlarging the nozzle throat diameter and that it typically occurred under relatively high-pressure circumstances. The findings of their study show that even at chamber pressures regularly found in traditional HRMs of a similar scale, axial-injection EBHRs may attain extraordinarily high fuel regression rates. Additionally, the O/F can be maintained almost constantly during firing, reducing the performance losses caused by an alteration in the O/F.

The problem of mixture ratio changes during firing, considered a barrier to the practical use of conventional hybrid rockets, has been demonstrated to be resolved by axial-injection EBHRs. Additionally, earlier research on regression rates in EBHRs operating at low pressures produced empirical formulas that projected solid fuel

regression rates higher than those anticipated from solid rocket motors operating at comparable pressures.

To ensure a consistent thrust in an end-burning hybrid engine, Rice et al. (2003) developed the vortex end-burning hybrid engine (VEBH), which maintains a consistent combustion area. The engine's O/F (fuel surface area) can be controlled by adjusting the combustion chamber diameter or oxidiser mass flow rate.

To enhance the fuel regression rate, the gaseous oxidiser is injected tangentially through ports located at the rear end of the chamber, inducing a swirling motion of the gas phase. This generates a flow field where two interwoven spirals spin in opposite directions toward the central nozzle, as depicted in Figure 2.6. Since the distance between the injection point and the fuel surface changes over time and may affect combustion stability and ignition, this idea is incompatible with the prolonged burn times needed for satellite applications.

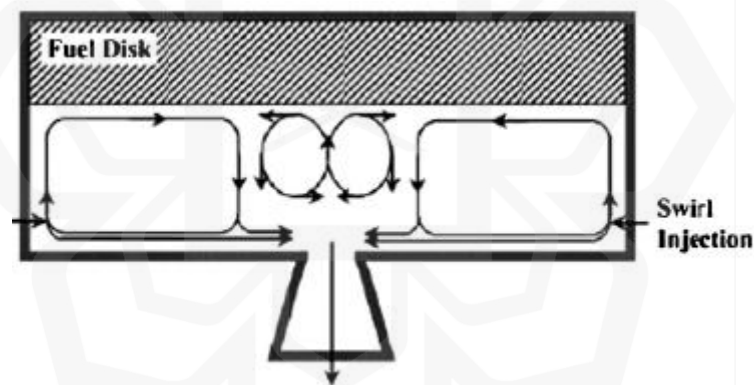


Figure 2.6 Flow field in the combustion chamber (Lestrade et al., 2019)

To gain a better understanding of the functioning of the innovative combustion chamber and to evaluate its effectiveness in achieving mission objectives, Lestrade et al. (2019) designed and conducted a preliminary test rig. The purpose of this test rig was to demonstrate the catalytic ignitability of the new hybrid engine and the ability to maintain stable combustion for firing durations of up to 180 seconds. Two test campaigns were carried out to achieve these goals. The first campaign involved testing the rig with 87.5% hydrogen peroxide, while the second campaign utilized the

hybrid engine breadboard with 98% hydrogen peroxide. These test campaigns were conducted under various operating conditions.

The primary objective of these tests was to identify the critical factor that influences the fuel regression rate in the novel combustion chamber. By analyzing the results obtained from the test rig and the hybrid engine breadboard, the researchers aimed to gain insights into the performance and characteristics of the combustion chamber, specifically in terms of catalytic ignitability, combustion stability, and fuel regression rate. These findings would contribute to the further development and optimization of the novel engine design.

The MHYCAS facility was the first, and it was created to help researchers better understand how this novel combustion chamber operates. The test program, carried out with hydrogen peroxide diluted to 87.5%, was effective and completed all its intended goals. The investigation showed that the key factors affecting the fuel regression rate are the number of active decomposition chambers and the oxidiser mass flux. The combustion chamber pressure has no discernible effect on this regression rate. The MHYCAS engine's drawing can be seen in Figure 2.7, and the engine's firing data can be seen in Table 2.4.

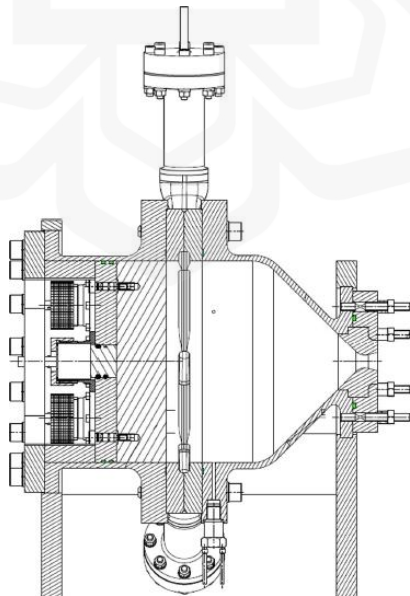


Figure 2.7 Drawing of the MHYCAS engine (Lestrade et al., 2019)

Table 2.4 MHYCAS firing test results (Lestrade et al., 2019)

MHYCAS test number	02	05	07	09	12	15	16	17	22
Number of active decomposition chambers	6	6	6	3	3	6	2	2	6
Oxidizer slot thickness (mm)	10.5	10.5	10.5	10.5	10.5	10.5	10.5	3.5	2.5
Ignition delay (s)	19.2	35.0	3.7	6.6	4.2	8.6	7.5	9.2	17.6
Firing duration (s)	12.7	18.0	28.8	36.2	29.1	23.8	25.3	22.9	16.0
Chamber pressure (bar)	7.87	8.24	17.89	8.54	18.26	11.03	7.67	7.02	5.62
Oxidizer mass flow rate (g/s)	51.7	52.1	103.1	41.4	44.1	107.9	36.2	30.6	30.3
Oxidizer mass flux (kg/m <sup>2</sup> /s)	16.4	16.5	37.7	26.3	28.0	34.3	34.4	87.5	40.4
Oxidizer-to-fuel mass ratio (-)	34.5	21.3	27.5	13.9	16.2	29.2	11.7	7.4	8.1
Regression rate (mm/s)	0.050	0.082	0.126	0.100	0.124	0.124	0.104	0.142	0.132
Experimental characteristic velocity (m/s)	1049	1071	1187	1364	1276	1212	1386	1436	1169
Combustion efficiency (%)	89.2	82.9	96.8	96.0	93.0	100.0	93.7	89.9	73.9

The outcomes of this initial test campaign made it possible to build the SuperMHYCAS hybrid engine, paying particular attention to the oxidiser injection to permit simple changes to the mass flux. The test campaign, which used hydrogen with a concentration of 98%, was likewise successful, with a combustion efficiency of roughly 90%. This can be regarded as satisfactory for the first engine of this size, which was not optimised for heat loss. As the firing duration increased, the averaged O/F firing tests decreased, most likely due to an escalation of the fuel regression rate's non-uniformity over the burning surface (Lestrade et al., 2019). The SuperMHYCAS engine's drawing can be shown in Figure 2.8, and the engine's firing data can be seen in Table 2.5.

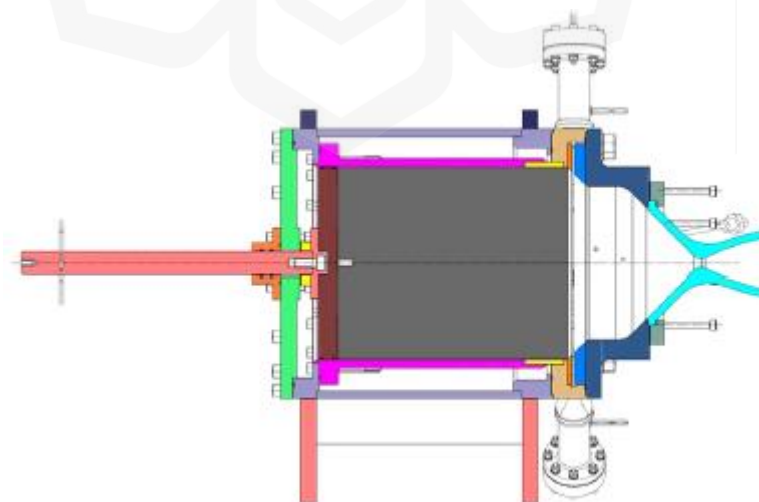


Figure 2.8 Drawing of the SuperMHYCAS engine (Lestrade et al., 2019)

Table 2.5 SuperMHYCAS test results (Lestrade et al., 2019)

SuperMHYCAS test number	05	06	07
Slor thickness (mm)	0.6	2.8	0.3
Ignition delay (s)	9.7	7.2	22.5
Firing duration (s)	45.3	47.8	32.5
Chamber pressure (bar)	8.43	8.00	7.27
Oxidizer mass flow rate (g/s)	51.4	53.5	46.4
Decomposition temperature (K)	1176	1190	1188
Oxidizer-to-fuel mass ratio (-)	5.1	9.3	4.1
Regression rate (mm/s)	0.221	0.125	0.243

Work done by Hitt (2020) gives additional findings from preliminary research by investigating the usage of fuel grains created via fused deposition modelling. Given that it prints layers utilising a filament extrusion process rather than curing photopolymers as in stereolithography, fused deposition modelling was intriguing. Fused deposition modelling is an accessible and affordable additive manufacturing method since it uses an extrusion process to print with various plastics.

In the initial test campaign, 22 test articles were fired. 13 of the test articles produced valuable outcomes. Other test products were disqualified for burn-through, excessive side-burning, or upstream flame propagation. Table 2.6 provides an overview of the outcomes for the baseline showing chamber pressure, oxidiser flow rate, and regression rate.

Table 2.6 ABS experimental results (Hitt, 2020)

Test article	Chamber pressure, kPa	Chamber pressure uncertainty, %	GOX mass flow rate, g/s	GOX mass flow rate uncertainty, %	Regression rate, mm/s	Regression rate uncertainty, %
32	444.4	0.3	6.5	3.8	1.98	3.7
33	423.1	0.3	12.3	3.8	1.67	3.7
34	335.7	0.4	9.7	3.8	1.33	3.8
36	202.8	0.8	6.4	3.8	0.48	4.1
38	121.1	1.4	3.8	3.9	0.14	9.2
39	123.2	1.4	16.5	3.8	0.44	4.7
41	161.0	1.0	21.8	3.8	1.26	3.8
42	169.8	1.0	24.0	3.8	1.15	3.8
43	289.3	0.5	5.2	3.8	0.85	4.0
44	178.7	0.9	3.8	3.9	0.25	6.0
46	832.7	0.1	18.9	3.8	3.63	4.0
49	559.2	0.2	18.9	3.7	1.28	4.3
50	470.7	0.3	16.7	3.8	1.03	4.5

Based on the baseline results, similar to other axial-injection, EBHR motor experiments, the chamber pressure affects the regression rate. Additionally, these fuel grains produce a fuel mass flux similar to earlier studied sintered-type, axial injection, EBHR motors. A volumetrically smaller fuel grain is possible using additive manufacturing due to the ability to sustain the fuel mass flux improvement found in sintered-type axial-injection, EBHR motors.

The work by Miwa et al. (2020) examines the applicability of RT2, one of the reconstruction techniques classified by Nagata et. al (2014) for EBHR and the reliability of the chamber pressure exponent for fuel regression rate at high chamber pressure stated by Okutani et al. (2018). The characteristic exhaust velocity efficiency  $\eta_{c^*}$  is assumed to be constant in RT2. As shown in Figure 2.9, a visualisation chamber with a polymethyl methacrylate (PMMA) window serving as an optical channel was employed to measure the flame moving velocity directly.

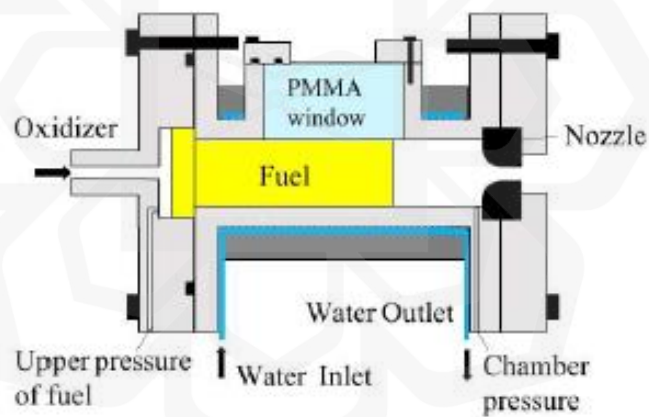


Figure 2.9 Visualisation chamber (Miwa et al., 2020)

Twenty-five firing tests were carried out to examine the applicability of the reconstruction method, and steady combustion was accomplished in 7 of them. Table 2.7, where  $d_{design}$  and  $d$  are the designed and measured port diameter, respectively, summarises fuel parameters for the seven fire tests. Table 2.8 lists the firing parameters and the results.

Table 2.7 Fuel parameters (Miwa et al., 2020)

Test	$d_{design}$ [mm]	$N$ [-]	$L$ [mm]	$d$ [mm]	$\alpha$ [-]	$B_d$ [mm]	$B_a$ [-]
1	0.50	151	107	0.479	0.976	$5.63 \times 10^{-3}$	$5.72 \times 10^{-4}$
2	0.50	151	107	0.466	0.977	$4.96 \times 10^{-3}$	$4.95 \times 10^{-4}$
3	0.50	151	107	0.457	0.978	$4.63 \times 10^{-3}$	$4.57 \times 10^{-4}$
4	0.50	151	107	0.467	0.977	$5.10 \times 10^{-3}$	$5.10 \times 10^{-4}$
5	0.40	235	107	0.382	0.976	$1.54 \times 10^{-2}$	$1.95 \times 10^{-3}$
6	0.50	151	107	0.480	0.976	$5.69 \times 10^{-3}$	$5.79 \times 10^{-4}$
7	0.50	151	107	0.487	0.975	$6.03 \times 10^{-3}$	$6.18 \times 10^{-4}$

Table 2.8 Firing conditions and results (Miwa et al., 2020)

Test	$D_t$ [mm]	$t_f$ [s]	$\dot{m}_o$ [g/s]	$P_c$ [MPa]	$M_{f_{CureableResin}}$ [g]	$M_{f_{PMMA}}$ [g]	$\eta_{c^*RT2}$ [-]	$\eta_{c^*JRT}$ [-]	$V_{f,RT2}$ [mm/s]	$V_{f,vis}$ [mm/s]	$\tau_{unsteady}$ [-]
1	6.6	40.1	6.7	0.25	40.97	3.00	0.83	0.87	0.94	0.911	0.50
2	6.2	33.9	6.0	0.35	67.89	3.49	0.88	0.88	2.53	2.60	0.38
3	6.2	17.2	5.8	0.37	33.91	1.10	0.88	0.88	1.67	1.70	0.21
4	6.2	25.0	5.1	0.37	45.31	1.54	0.92	0.90	1.70	1.79	0.60
5	7.0	44.3	9.6	0.37	83.60	5.18	0.89	0.89	1.43	1.46	0.21
6	6.2	9.8	11.5	0.88	52.39	0.65	0.78	0.80	6.24	5.86	0.82
7	6.2	7.8	15.0	1.27	64.98	0.72	0.78	0.83	12.4	9.64	0.90

In tests with chamber pressures under 0.5 MPa, the fuel regression rate calculated by RT2 agreed with the flame travelling velocity determined by visualisation; however, RT2 overestimated the fuel regression rate in tests with chamber pressures above 0.9 MPa or so, and this discrepancy grew as chamber pressure increased. Utilising direct visualisation-derived histories of the moving velocity of flames, a novel data reduction technique known as inverse RT derives  $\eta_{c^*}$  histories. Additionally, it was discovered that the RT2 findings for  $\eta_{c^*}$  vary between pressure-steady-state and pressure-unsteady-state times by performing RT2 individually for each during a single firing test.

In this instance, the pressure unsteady state's value of  $\eta_{c^*}$  was lower than the pressure steady state's value. This suggests that the RT2 overestimates the fuel regression rates of the pressure steady-state timings because it underestimates  $\eta_{c^*}$ . In addition, the ratio of the pressure-unsteady-state duration to the firing duration is higher in high-chamber pressure tests than in low-chamber pressure testing. This indicates that, compared to low chamber pressure testing, the time-varying  $\eta_{c^*}$  has a more direct impact on the entire combustion.

## 2.8 HIGH ENTROPY ALLOY

HEAs are alloys composed of five or more main elements, with the concentration of each primary component typically ranging from 5 to 35% (Tsai & Yeh, 2014). Besides the primary elements, HEAs may contain minor elements, each present in a percentage below 5%. These alloys are referred to as "HEAs" because they exhibit significantly higher mixing entropies in their liquid or solid solution phases compared to conventional alloys. As a result, the influence of entropy is more pronounced in HEAs. However, there is a debate regarding the classification of multi-component alloys as HEAs due to conflicting definitions based on composition and entropy (Zhang et al., 2018).

### 2.9.1 Definitions

Zhang et al. (2018) stated that the first composition-based definition appeared in a publication in 2004. At least five principal elements, each having an atomic proportion between 5 and 35%, were required to define HEAs. The atomic composition of minor elements, if present, is less than 5%. The following is how the definition is stated (Zhang et al., 2018):

$$n_{\text{major}} \geq 5, 5 \text{ at.}\% \leq c_i \leq 35 \text{ at.}\% \\ \text{and } n_{\text{minor}} \geq 0, c_j \leq 5 \text{ at.}\%$$

Where the numbers of the major and minor elements are indicated by  $n_{\text{major}}$  and  $n_{\text{minor}}$ , respectively. The atomic percentages of the major element,  $i$  and the minor element,  $j$ , are denoted by the letters  $c_i$  and  $c_j$ . According to this definition, HEAs do not necessarily need to be equimolar or nearly equimolar. They can even contain minor components to balance out different material qualities like ductility, toughness, strength, creep, oxidation, etc. (Zhang et al., 2018).

The essence of entropy, a thermodynamic state function, is the system's "inherent chaos" (Zhang et al., 2018). According to Boltzmann's thermodynamic statistics principle, the system's entropy and randomness have the following quantitative relationship:



$$\Delta S_{conf} = k \ln w$$

Where  $w$  is the number of distinct ways to arrange the atoms in the solution and  $k$  is Boltzmann's constant. The total mixing entropy has four contributions: configurational entropy,  $\Delta S_{mix}^{conf}$ , vibrational entropy,  $\Delta S_{mix}^{vib}$ , magnetic dipole entropy,  $\Delta S_{mix}^{mag}$ , and electronic randomness entropy,  $\Delta S_{mix}^{elec}$ , and the relationship among them is given by:

$$\Delta S_{mix} = \Delta S_{mix}^{conf} + \Delta S_{mix}^{vib} + \Delta S_{mix}^{elec} + \Delta S_{mix}^{mag}$$

In comparison to the other three contributions, configurational entropy is dominant. Because of this, it is typical for the configurational entropy to serve as a proxy for the mixing entropy to avoid tedious calculations to determine the other three components (Zhang et al., 2018). According to Zhang et al. (2018), an ideal random  $n$ -component solid solution has approximately the following ideal configurational entropy per mole:

$$\begin{aligned} \Delta S_{conf} &= -R[c_1 \ln c_1 + \dots + c_n \ln c_n] \\ &= -R \sum_{i=1}^n c_i \ln c_i \end{aligned}$$

Where  $R$  is the gas constant,  $c_i$  is the mole fraction of the  $i^{th}$  element, and  $n$  is the number of the components. The extreme theorem states that the system's entropy achieves its greatest value when  $c_1 = c_2 = \dots = c_n$ . An equiatomic alloy's configurational entropy per mole could be computed by considering its liquid state or normal solid-solution state (Zhang et al., 2018):

$$\Delta S_{conf} = R \ln n$$

It states that HEAs, whether single-phase or multiphase at room temperature, have a configurational entropy in a random state greater than  $1.5R$ . This definition, according to Zhang et al. (2018), could be stated as follows:

$$\Delta S_{conf} > 1.5R$$

## 2.9.2 Core Effects

The multi-principal-element nature of HEAs brings about some significant impacts that are far less noticeable in ordinary alloys. These four impacts

might be regarded as the core effects. The main impacts are briefly described and discussed in this section.

1. High-Entropy Effect

The high entropy effect, which is the core idea of HEAs, presumes that in near-equimolar alloys containing five or more elements, increasing configurational entropy may favour solid solution (SS) phases over rival intermetallic (IM) compounds. Miracle & Senkov (2016) claim that to support this viewpoint, idealised configurational entropy is contrasted with the entropy of fusion for pure metals or with the formation enthalpies of certain IM compounds.

2. Sluggish Diffusion Effect

It is hypothesised that diffusion in HEAs is slow (Miracle & Senkov, 2016). This assertion is supported by secondary data, including the solidification-induced creation of nanocrystals and amorphous phases, as well as qualitative interpretations of the stability of the microstructure after cooling.

3. Severe Lattice Distortion Effect

The varied atom sizes that make up the crystal lattices of complex, condensed phases cause severe lattice distortion. Every atom in the local surroundings and the sorts of atoms at each lattice site affect the displacement at that location. It is asserted that these aberrations are more severe than in standard alloys. X-ray diffraction peak intensity, hardness, electrical and thermal conductivity, and the temperature dependence of these properties are all said to be decreased by the uncertainty in atom locations caused by these distortions, according to Miracle & Senkov (2016).

4. Cocktail Effect

Prof. S. Ranganathan coined the colourful and evocative term "cocktail effect" (Miracle & Senkov, 2016). The phrase "a delightful, enjoyable mixture," which he originally intended to

mean, later came to refer to a synergistic blend in which the final product is unpredictable and larger than the sum of the parts (Miracle & Senkov, 2016). Three different alloy classes were introduced using this term: bulk metallic glasses, super-elastic and super-plastic metals, sometimes known as "gum metals," and HEAs. These alloy classes each contain concentrated, intricate alloy compositions. The "cocktail" effect considers the highly extreme structural and functional features of "gum" metals and the fantastic properties of totally amorphous bulk metallic glasses.

### 2.9.3 Preparation of HEAs

The manufacture of HEAs follows in the footsteps of the three main approaches that can be used to create amorphous alloys, as indicated in Figure 2.10 (Zhang et al., 2018).

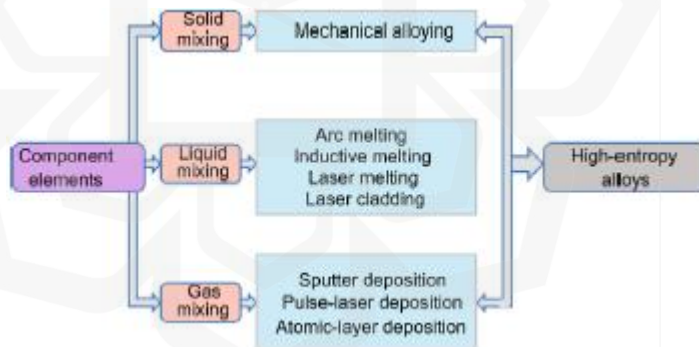


Figure 2.10 Fabrication routes of HEAs (Zhang et al., 2018)

Liquid mixing is the primary method used in various processes, such as arc melting, electric resistance melting, inductive melting, laser melting, laser cladding, and laser-engineered net shaping (LENS) (Zhang et al., 2018). These techniques involve the incorporation of liquid materials through different means to achieve desired outcomes. The second approach is solid mixing, which primarily involves the process of mechanical alloying followed by consolidation. This method focuses on blending solid materials through

mechanical means to create desired compositions. Another pathway is gas mixing, which encompasses techniques such as sputter deposition, pulse-laser deposition (PLD), atomic layer deposition (ALD), molecular-beam epitaxy (MBE), and vapour-phase deposition. These methods involve the use of gases to deposit or grow thin films or coatings onto substrates (Zhang et al., 2018). Arc melting is the most common fabrication technique for producing bulk HEAs among the listed preparatory techniques.

#### **2.9.4 Properties of HEAs**

The properties of HEAs can vary significantly due to the wide range of compositions and numerous alloy systems available. The information provided in this paragraph is based on findings from Zhang et al. (2018).

##### **1. Hardness**

HEAs have been extensively studied due to their remarkable hardness and strength, as well as their formation of a single multi-component solid-solution phase. Figure 2.11 illustrates the hardness of various alloys in both their as-cast and fully annealed states. It is observed that HEAs exhibit higher hardness and superior resistance to softening during annealing compared to conventional alloys such as Hastelloy C and 316 stainless steel.

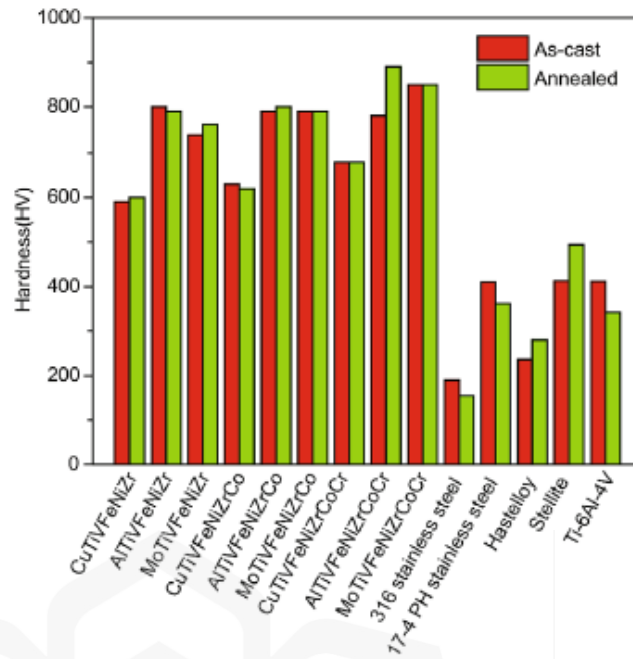


Figure 2.11 HEAs and conventional alloys' hardness comparison before and after annealing (Zhang et al., 2018)

## 2. Compressive property

Compressive loading on cylindrical samples easily generated by arc melting is used to assess the mechanical properties of HEAs. Compared to those with a body-centred-cubic (BCC) phase, as shown in Figure 2.12, HEAs systems typically have a face-centred-cubic (FCC) phase and superior strength and ductility in compression. However, HEAs with a BCC phase have extremely high yield strengths that are on par with bulk metallic glasses. Due to solid-solution hardening and decreased ductility, the strength of the HEAs system increases with the number of major elements (Zhang et al., 2018). In the FCC matrix, creating a BCC phase reduces ductility while increasing compressive strength.

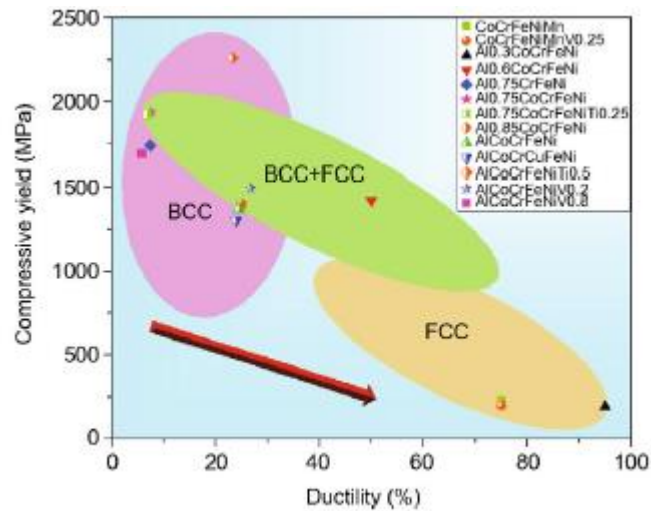


Figure 2.12 Compressive behaviour of various HEAs (Zhang et al., 2018)

### 3. Tensile property

The tensile characteristics of HEAs were the subject of few studies. Zhang et al. (2018) indicate that the HEAs' crystal structure significantly affects their tensile characteristics. Compared to typical superalloys and stainless steels, the superior mechanical properties of HEAs throughout a wide range of temperatures under tensile loading make them attractive candidates for structural applications.

### 4. Corrosion resistance

HEAs exhibit exceptional corrosion resistance when exposed to high concentrations of sulfuric acid, hydrochloric acid, nitric acid, and other corrosive solution conditions (Zhang et al., 2018). Some HEAs exhibit exceptional corrosion resistance that surpasses that of conventional stainless steel. In contrast to Al-, Cu-, and some Ti-based alloys, HEAs have higher pitting potential ( $E_p$ ) and lower corrosion current densities ( $I_{corr}$ ), according to Figure 2.13 from Zhang et al. (2018). The HEAs exhibit superior localised and overall corrosion resistance as a result.

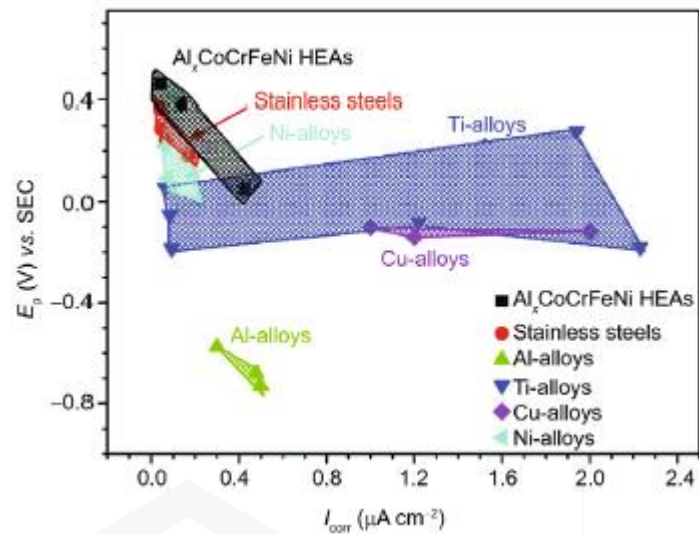


Figure 2.13 Comparison of  $E_p$  and  $I_{corr}$  between HEAs of  $Al_xCoCrFeNi$  ( $x = 0.3, 0.5, \text{ and } 0.7$ ) and other conventional alloys in 3.5 wt% NaCl solution at room temperature (Zhang et al., 2018)

#### 5. Thermal stability

Refractory HEAs are a new class of multi-component alloys with outstanding mechanical characteristics at high temperatures (Zhang et al., 2018). These outstanding characteristics of HEAs enable a new class of materials in nanoscale devices that may be used in high-stress and high-temperature applications.

#### 6. Irradiation property

The study demonstrates that the HEAs exhibits high phase stability even with an Au ion irradiation dose greater than 50 dpa (displacement per atom). HEAs has a relatively low volume swelling rate at the same irradiation dose of 50-70 dpa compared to other frequently used irradiation-resistant materials, like M316 stainless steel and pure Zr. High-performance HEAs radiation-resistant materials offer a fresh perspective on nuclear materials and have been a driving force behind the nuclear energy industry (Zhang et al., 2018).

## 7. Thermoelectric property

The high degree of chaos in HEAs' atomic structure enhances phonon scattering and significantly lowers the material's lattice thermal conductivity. The lattice thermal conductivity of the PbSnTeSe HEAs, which has a temperature-dependent value of  $0.6 \text{ Wm}^{-1}\text{K}^{-1}$ , was discovered. The thermoelectric performance of PbSnTeSe might be further improved by small additions of La to replace Pb, as seen in Figure 2.14.

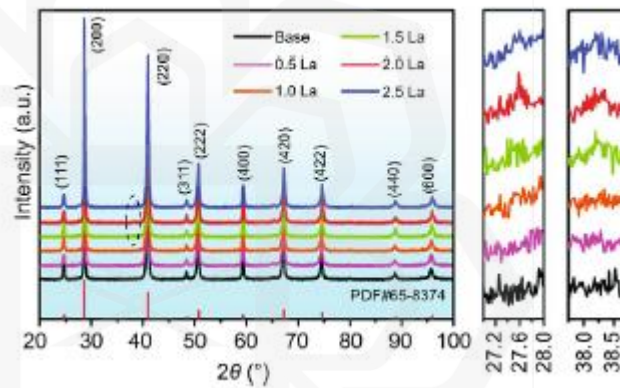


Figure 2.14 XRD patterns of  $\text{Pb}_{1-x}\text{SnTeSeLa}_x$  HEAs (Zhang et al., 2018)

## 8. Other properties

According to Zhang et al. (2018), HEAs possess outstanding wear resistance, fracture toughness, high resistivity, and good soft magnetic characteristics.

### 2.9.5 The Al-Co-Cr-Cu-Fe-Ni Alloy System

The Al-Co-Cr-Cu-Fe-Ni and Cu-free Al-Co-Cr-Fe-Ni systems have been extensively studied among various High Entropy Alloy (HEA) systems (Tsai & Yeh, 2014), making them the most researched HEAs. The main distinction



lies in the presence of a Cu-rich interdendrite. This distinction arises because copper (Cu) has a tendency to accumulate in the interdendrite region and forms favorable interactions with many other elements.

When the Al-Co-Cr-Cu-Fe-Ni alloy is cast, it consists of three primary phases: face-centered cubic (FCC), body-centered cubic (BCC) or B2, and the Cu-rich phase, which also adopts an FCC structure. The relative volume ratio of these phases is influenced by the alloy's composition. The valence electron concentration (VEC) of the alloy is closely related to the relative volume of the BCC and FCC phases. Higher VEC often leads to a larger fraction of the FCC phase, and vice versa. Aluminum (Al) has the most significant impact in this regard, as its presence causes the FCC phase to transform into the BCC phase. A (Cr, Fe)-rich BCC phase and an (Al, Ni)-rich B2 phase with nearly identical lattice characteristics tend to form from BCC when enough Al is present. When the concentration of Cu is more than 10%, the Cu-rich phase is clearly visible. Its fraction rises with an increase in Cu concentration (Tsai & Yeh, 2014).

The FCC phase's average hardness ranges from HV 100 to 200 (Tsai & Yeh, 2014). Alloys containing a solitary FCC phase have between 20 and 60% ductility and frequently display severe work hardening. The hardness of the BCC/B2 phase is generally between HV 500 – 600 because the inclusion of Al promotes the formation of a hard BCC/B2 phase, and the hardness of the alloy rises with Al's presence. Alloys that primarily consist of a BCC or B2 phase typically exhibit less than 5% ductility. However, in terms of their flexibility, values of 30% or higher have been reported (Tsai & Yeh, 2014). Notably, the AlCoCrCuFeNi alloy has demonstrated superplastic behavior at temperatures around 800-1000°C, with elongation values ranging from 405% to 800%.

According to Tsai & Yeh (2014), the mechanical characteristics of the Al-Co-Cr-Cu-Fe-Ni system are influenced by annealing processes, which are dependent on phase transformations. The alloy becomes more brittle and tougher when the annealing temperature encourages the formation of the BCC phase. On the other hand, selecting a higher temperature that increases the fraction of the FCC phase leads to alloy softening and increased ductility. It is

important to note that prolonged annealing in this alloy system can result in the formation of a phase that increases alloy hardness but significantly reduces its ductility and plasticity.

## **2.10 CONCLUDING REMARKS**

Researchers looking for a substitute for the complexity of liquid-propellant rockets and the explosive dangers of solid-propellant rockets began developing hybrid rocket technology in the 1930s. As a result of their safety, affordability, throttling capability, and expanded propellant range, HRMs have gained popularity in recent years. The low regression rate of this type of rocket is its principal drawback. Many strategies were used to address this issue, and end-burning combustion mode was one of them. Also highlighted were HEAs, alloys containing five or more primary elements, which have garnered much attention across various sectors. HEAs outperforms standard alloys in strength and hardness, corrosion resistance, thermal stability, fatigue resistance, fracture resistance, and irradiation resistance due to their many primary components and unique microstructures. All these characteristics have given HEAs a wealth of exciting prospective applications.

# CHAPTER 3

## METHODOLOGY

### 3.1 INTRODUCTION

This section will discuss the research methodology employed to investigate the efficiency of an EBHR. An experimental approach will be utilized to analyse the regression rate of the EBHR. The initial step involves determining the constants of the fuel and oxidiser to design and manufacture the EBHR. The results obtained from laboratory-scale tests will be documented. Subsequently, the regression rate of the EBHR will be examined and assessed. Figure 3.1 shows how the study proceeded.

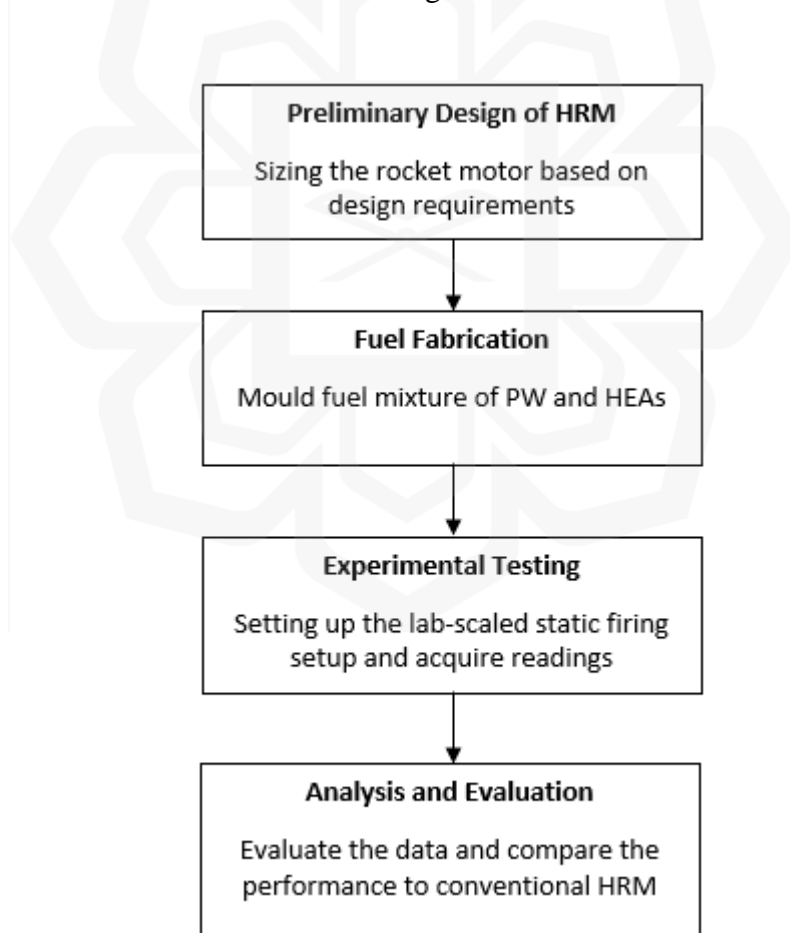


Figure 3.1 Research methodology flowchart

### 3.2 PRELIMINARY DESIGN OF AN EBHR

The initial design of the hybrid rocket was based on a model by Humble et al. (1995). The design process begins by estimating the mixture density of the propellant and selecting the essential design requirements and appropriate design margins. Thermochemical evaluation is then conducted to determine the ideal O/F based on factors such as specific heat ratio, flame temperature, and propellant's characteristic velocity (Humble et al., 1995).

During the design module, it is assumed that the oxidiser mass flow rate are unchanged during combustion, and the regression rate remains constant at all burning sites. The design process flowchart is illustrated in Figure 3.2. The initial choices and assumptions made for the HRM design are presented in Table 3.1.

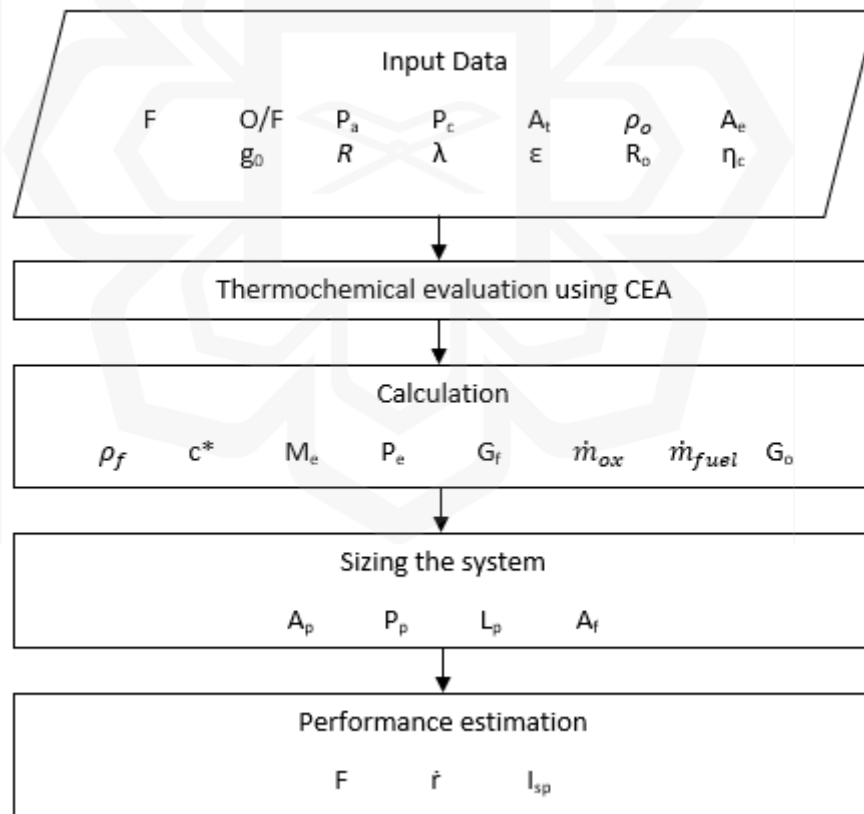


Figure 3.2 Preliminary design flowchart

Table 3.1 Preliminary decisions for HRM design

Initial thrust (vacuum), F [N]	50
Optimal initial O/F ratio	1.8
Ambient pressure, P <sub>a</sub> [Pa]	101325
Chamber pressure, P <sub>c</sub> [Pa]	500000
Oxygen density, ρ <sub>o</sub> [kg/m <sup>3</sup> ]	1.429
Nozzle exit area, A <sub>e</sub> [m <sup>2</sup> ]	0.001260
Nozzle throat area, A <sub>t</sub> [m <sup>2</sup> ]	0.000079
Gravitational acceleration constant, g <sub>0</sub> [m/s <sup>2</sup> ]	9.81
Nozzle expansion ratio, ε	3
Nozzle efficiency, λ	0.65
Gas Constant, R [J/kg.K]	287
Combustion efficiency, η <sub>c</sub>	1
Fuel grain outside radius, R <sub>o</sub> [m]	0.0215

The optimal specific heat ratio,  $\gamma$ , molar masses,  $M$ , as well as the flame temperature,  $T_f$ , are determined using the curve fit obtained from the experimental data presented by Humble et al. (1995).

$$\gamma = 0.0067\left(\frac{O}{F}\right)^4 - 0.0786\left(\frac{O}{F}\right)^3 + 0.3487\left(\frac{O}{F}\right)^2 - 0.7034\left(\frac{O}{F}\right) + 1.7683 \quad (2)$$

$$M = 0.3094\left(\frac{O}{F}\right)^6 - 4.631\left(\frac{O}{F}\right)^5 + 28.23\left(\frac{O}{F}\right)^4 - 89.006\left(\frac{O}{F}\right)^3 + 150.56\left(\frac{O}{F}\right)^2 - 121.7\left(\frac{O}{F}\right) + 52.301 \quad (3)$$

$$T_f = 91.701\left(\frac{O}{F}\right)^6 - 1380.9\left(\frac{O}{F}\right)^5 + 8355.5\left(\frac{O}{F}\right)^4 - 25592.0\left(\frac{O}{F}\right)^3 + 40466.0\left(\frac{O}{F}\right)^2 - 28680.0\left(\frac{O}{F}\right) + 8407.4 \quad (4)$$

The characteristic velocity,  $c^*$ , is determined using the specific heat ratio, molar mass, and flame temperature values.

$$c^* = \frac{\eta_c \sqrt{\gamma R T_f}}{\gamma \left(\frac{2}{\gamma+1}\right)^{\frac{\gamma}{\gamma-1}}} \quad (5)$$

The parameter of the fuel mix containing HEAs is calculated using the formulas below:

$$\frac{1}{\rho_{mixture}} = \frac{X_f}{\rho_f} + \frac{X_{Additives}}{\rho_{Additives}} \quad (6)$$

$$C_{p,mixture} = \left( \frac{m_{fuel}}{m_{mixture}} \right) C_{p,fuel} + \left( \frac{m_{additives}}{m_{mixture}} \right) C_{p,additive} \quad (7)$$

$$K_{mixture} = K_{fuel}V_{fuel} + K_{additives}V_{additives} \quad (8)$$

The nozzle exit Mach number,  $M_e$ , is computed using the relationship derived from the expansion ratio.

$$\varepsilon = \frac{1}{M_e} \sqrt{\left[ \frac{2}{\gamma+1} \left( 1 + \frac{\gamma-1}{2} M_e^2 \right) \right]^{\frac{\gamma+1}{\gamma-1}}} \quad (9)$$

The exit pressure,  $P_e$ , is calculated using the isentropic relation.

$$P_e = \frac{P_c}{\left( 1 + \frac{\gamma-1}{2} M_e^2 \right)^{\frac{\gamma}{\gamma-1}}} \quad (10)$$

The specific impulse,  $I_{sp}$ , is obtained by applying the following equation:

$$I_{sp} = \lambda \left\{ \frac{c^* \gamma}{g_0} \sqrt{\left( \frac{2}{\gamma-1} \right) \left( \frac{2}{\gamma+1} \right)^{\frac{\gamma+1}{\gamma-1}} \left[ 1 - \left( \frac{P_e}{P_c} \right)^{\frac{\gamma-1}{\gamma}} \right]} + \frac{c^* \varepsilon}{g_0 P_c} (P_e - P_a) \right\} \quad (11)$$

The total propellant mass flow rate,  $\dot{m}_{propellant}$ , is dependent on the desired initial thrust,  $F$ , and can be obtained from the equation below:

$$F = \dot{m}_{propellant} I_{sp} g_0 \quad (12)$$

The mass flow rates of the fuel,  $\dot{m}_f$ , and oxidiser,  $\dot{m}_o$ , can then be calculated using the given relationship:

$$\dot{m}_f = \frac{\dot{m}_{propellant}}{1 + \frac{O}{F}} \quad (13)$$

$$\dot{m}_o = \dot{m}_{propellant} - \dot{m}_f \quad (14)$$

The oxidiser inlet velocity,  $V_i$ , is obtained below:

$$V_i = \sqrt{\frac{2(P_c - P_a)}{\rho_o}} \quad (15)$$

The port area,  $A_p$ , and fuel area,  $A_f$ , can be determined using the provided equations below.

$$A_p = \frac{\dot{m}_o}{\rho_o V_i} \quad (16)$$

$$A_f = \pi R_o^2 - A_p \quad (17)$$

The fuel regression rate,  $\dot{r}$ , is expressed as:

$$\dot{r} = \frac{\dot{m}_f}{\rho_f A_f} \quad (18)$$

The fuel regression and pressure exponent coefficient,  $a$  and  $n$ , can be empirically determined using the given equation:

$$\dot{r} = \alpha P_c^n \quad (19)$$

### 3.3 EXPERIMENTAL SETUP

This section depicts the lab-scale development of an EBHR. The lab-scale HRM testing facility can accommodate different fuel lengths. The test facility consists of the following: (1) casing, (2) fuel, (3) feed system, (4) ignition system, (5) feed and end caps, (6) nozzle, (7) data acquisition system and (8) testbed.

#### 3.3.1 Casing

Due to the low melting point of PW, it must be kept in a case. The casing specifications can be seen in Table 3.2. The arrangement of the fuel grains determines the length of the combustion chamber. The case utilised for this study is shown in Figure 3.3. PMMA, or polymethyl methacrylate, was selected as the preferred material due to its transparency, which provides a clear view of the combustion process. This transparency is beneficial for verifying the end-burning characteristics of the hybrid rocket.

Table 3.2 Casing specifications

Material	PMMA
Length [m]	0.17
Outer diameter [m]	0.045
Inner diameter [m]	0.043
Mass [kg]	0.0596

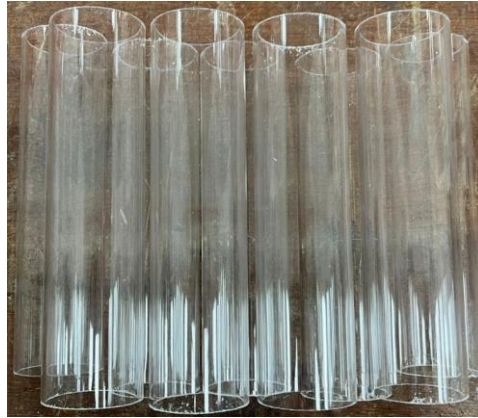


Figure 3.3 PMMA casing

### 3.3.2 Fuel

When selecting a fuel for the experiment, the primary consideration is the availability of materials. In this case, PW was chosen as it is widely accessible. Previous research has indicated that PW is particularly suitable for lab-scale hybrid rockets due to its ease of shaping. The specifications of the fuel used in the experiment can be found in Table 3.3. As depicted in Figure 3.4, a single circular port will be utilized throughout the duration of the experiment.

Table 3.3 PW fuel specifications

Material	PW
Length [m]	0.13
Outer diameter [m]	0.043
Inner diameter [m]	0.028
Mass [kg]	0.100

According to Arifah et al. (2023), since not all elements may be combined in a single system, it is crucial to ensure that the elements utilised in the HEAs solid solution are compatible. The Hume-Rothery rules for binary substitutional solid solutions are explored after recognising the prerequisite for



HEAs. The first Hume-Rothery rule can be strengthened by considering the degree of similarity between all the atomic sizes of the alloy's atoms because HEAs have more major primary elements than typical alloys (Arifah et al., 2023). The composition of the elements is selected to ensure a homogenous mixture. The elements used in this study are Iron (Fe), Cobalt (Co), Nickel (Ni), Aluminium (Al), Boron (B) and Silicon (Si) powders, as listed in Table 3.4.

Table 3.4 HEAs composition

Elements	Composition [wt.%]	Mass [g]
Fe	0.27	1.023
Co	0.27	1.080
Ni	0.27	1.077
Al	0.05	0.092
B	0.05	0.035
Si	0.1	0.215
Total		3.522

Table 3.5 and Figure 3.4 shows the properties of the fuel and the PW doped with HEAs. After the HEAs are prepared, the HEAs are weighed based on the weight of the PW, which is 0.1 kg.

Table 3.5 HEAs with PW

Parameters	PW + 3% HEA	PW + 5% HEA	PW + 7% HEA
Fuel mass, $m_f$ [kg]	0.103	0.105	0.107
Fuel density, $\rho_f$ [kg/m <sup>3</sup> ]	890.45	885.56	880.67
Specific heat, $C_p$ [J/kg.K]	2052.69	2021.13	1989.57
Thermal conductivity, $K$ [W/mK]	4.01	6.53	9.06

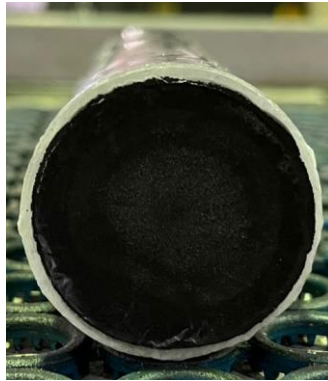


Figure 3.4 PW doped with HEAs

The PW grain was melted and poured into the PMMA casing. The HEAs was added and mixed thoroughly until the solution becomes almost homogenous. The port was created using a lathe turning machine with a 28 mm drill bit at the speed of 108 revolution per minute to ensure smooth surface with a tolerance of 0.1 mm. Figure 3.5 shows the fabrication process. The final product is presented in Figure 3.6 where it is stored in a desiccator to reduce exposure to moisture.



Figure 3.5 Fabrication process



Figure 3.6 Finished fuel

### 3.3.3 Feed System

Figure 3.7 shows the feeding system. The oxidiser used is a self-pressurised oxygen gas.

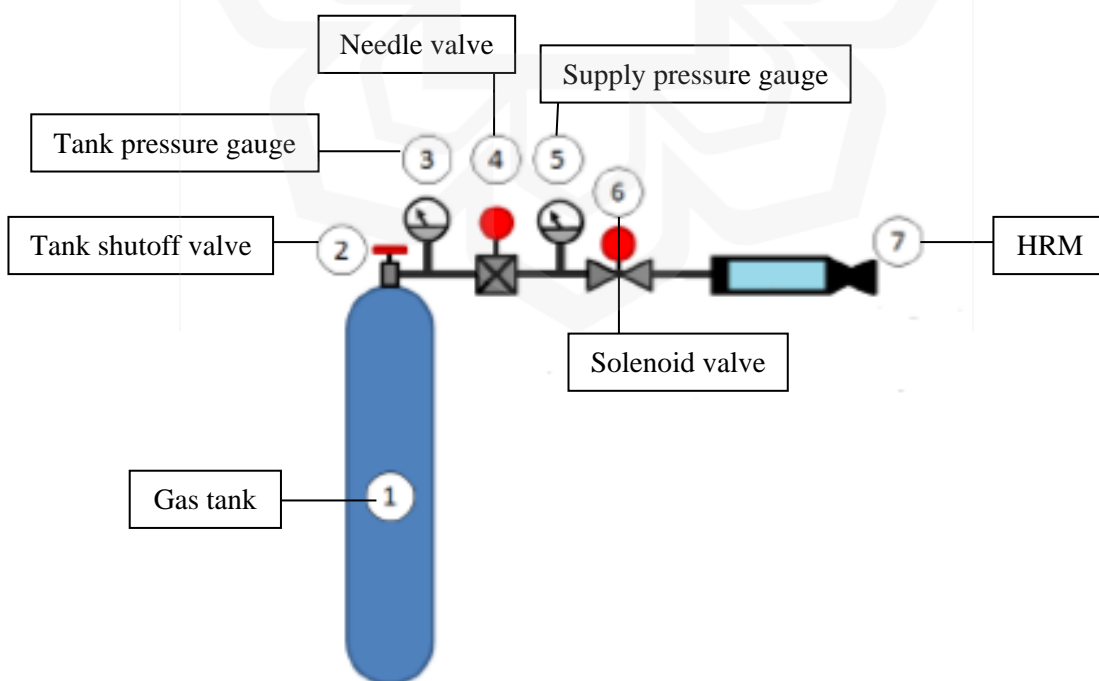


Figure 3.7 Feeding system diagram (Azami, 2014)

For ease of usage, the oxidiser was a 10 L GOX tank. Another factor is that it is more widely available and simple to refill than other oxidisers. Figure 3.8 - 3.10 display the elements.



Figure 3.8 Oxygen tank (left), pressure gauge and regulator (right)



Figure 3.9 Needle valve (left) and solenoid valve (right)



Figure 3.10 Feed line connection

The pressure regulator manages how much oxygen gas is released into the combustion chamber from the oxygen tank. A ball valve regulates the flow of oxidiser into the chamber.

### 3.3.4 Ignition System

To supply electricity to the igniter, a basic control system is used. Figure 3.11 shows the controller. The igniter system can be controlled remotely and have several safety features such as buzzer, switch key, and analogue toggle.

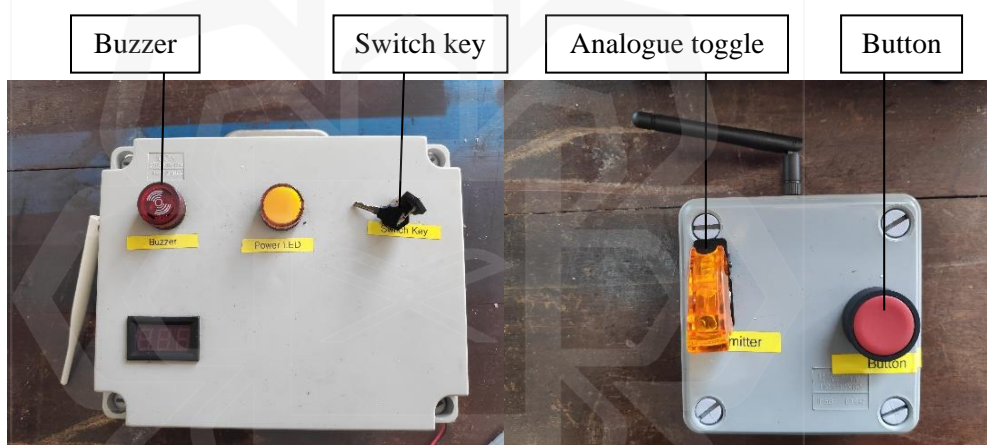


Figure 3.11 Igniter controller

Twin black and red wires, a switch, connectors, and matches are used; new wires must be added after every fire. Matches were used as the pyrogen and were heated using the steel coil. The steel coil is wired to a power source. When a current is delivered, the steel coil heats up and ignites the match. The item is displayed in Figure 3.12.

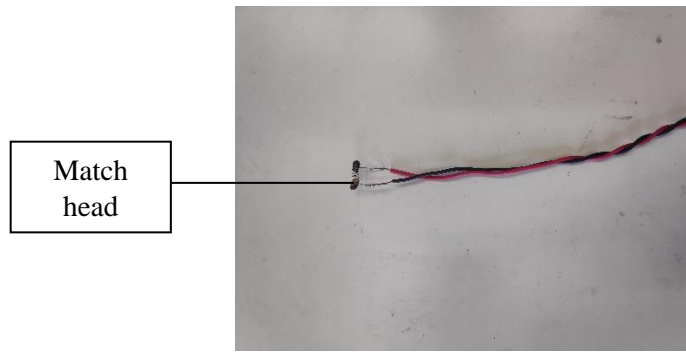


Figure 3.12 Igniter

### 3.3.5 Feed and End Caps

Feed and end caps with the sensors were installed at both ends of the fuels. Its primary tasks include clamping the fuel and providing a location for pre- and post-combustion. For installation, thermocouples and pressure transmitters were put on the top and sides of both caps. The caps are shown in Figure 3.13.



Figure 3.13 Feed cap (left) and end cap (right)

### 3.3.6 Nozzle

The nozzle is shown in Figure 3.14, and Table 3.6 shows the specifications.



Table 3.6: Nozzle specifications

Material	Aluminium
Length [m]	0.17
Type	Convergent-divergent nozzle
Throat diameter [m]	0.01
Expansion ratio	3.00

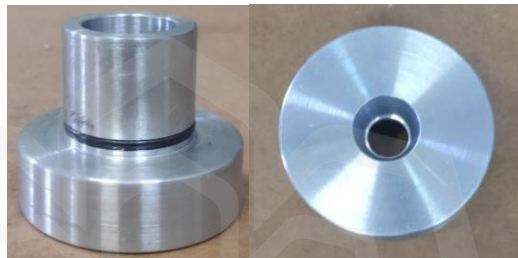


Figure 3.14 Nozzle

### 3.3.7 Data Acquisition System

The feed and end cap are where the thermocouple and pressure transmitter are installed. The testbed's front is where the load cell is attached. The red button act as an emergency shutdown. All the sensors are connected to the main box, as shown in Figure 3.15. The data from these sensors is transferred directly to the computer from the Arduino.

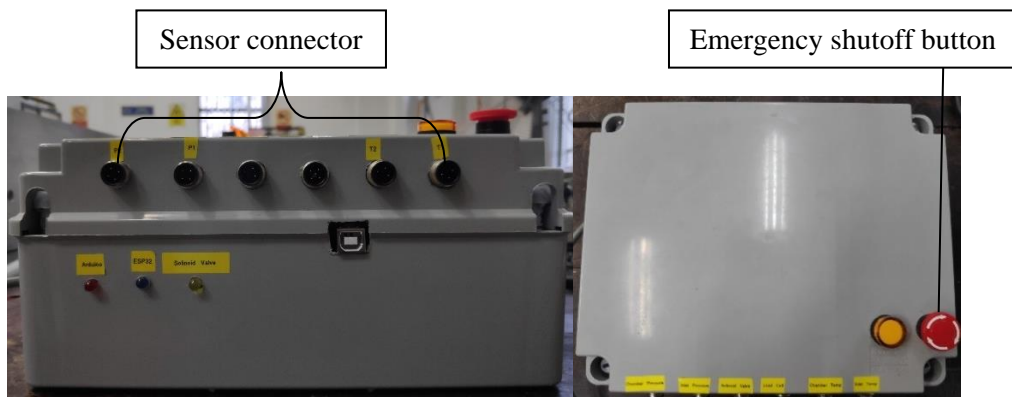


Figure 3.15 Data acquisition system

The installation of K-type WIKA TC40 industrial thermocouples sensors is shown in Figure 3.16. The sensors made of stainless steel can track temperatures as high as 1260 °C.

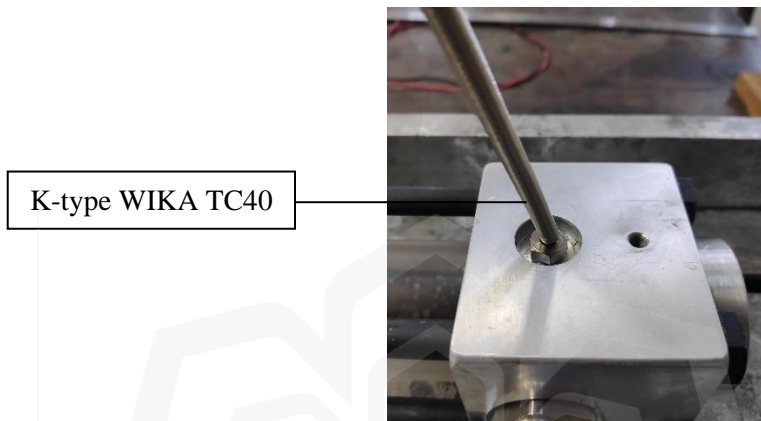


Figure 3.16 Thermocouples installation

The thrust is measured with the use of an S-typed load cell. It can be measured up to 1000 N. It is necessary to use an external power source and a battery. Up to 10 mV in output voltages was possible. Figure 3.17 shows the installation of a load cell.

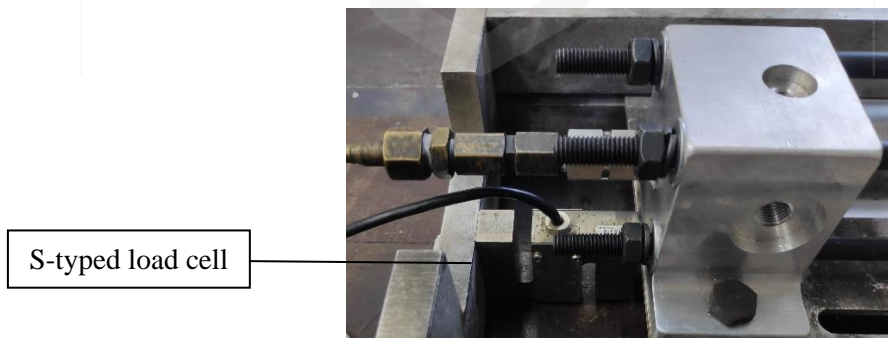


Figure 3.17 Load cell



The WIKA E-10 pressure transmitter has an explosion-proof housing. Since the output ranges from 4 to 20 mA, calibration is necessary. Stainless steel tube is required for cooling. This tube is directly connected to the end cap and the feed. The pressure transmitter is seen in Figure 3.18. The data acquisition system used by Arduino is shown in Figure 3.19.



Figure 3.18 E10 pressure transmitter



Figure 3.19 Arduino UNO R3

### 3.3.8 Testbed

Figure 3.20 shows the fabricated testbed, and the specifications are listed in Table 3.7. The clamping rods connects the feed and end caps and clamp the HRM. The rollers are underneath the testbed to provide smooth movement to the slider.

Table 3.7 Testbed specifications

Material	Aluminium
Length [m]	0.505
Width [m]	0.230
Height [m]	0.100

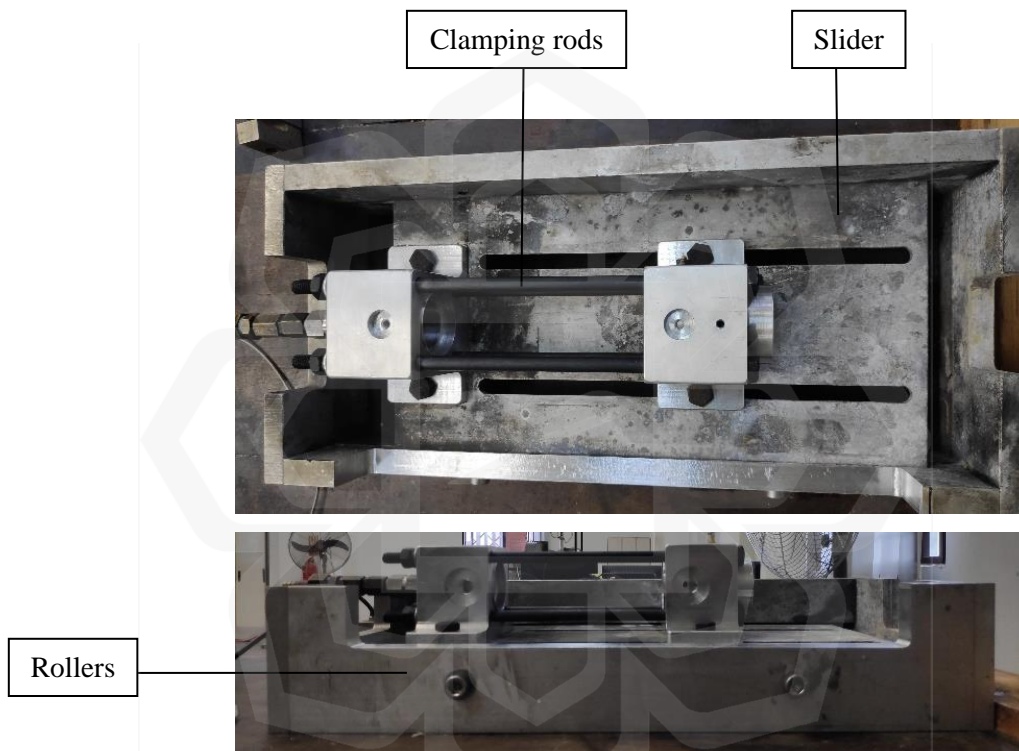


Figure 3.20 Testbed

### 3.3.9 Test Setup

Figure 3.21 illustrates the configuration used for this experiment. The GOX will be injected in an axial direction through the feed cap located at the front of the chamber. In order to facilitate end-burning, the igniter will be positioned at the end of the chamber. The experimental setup is covered with acrylic panel to act as a safety shield.

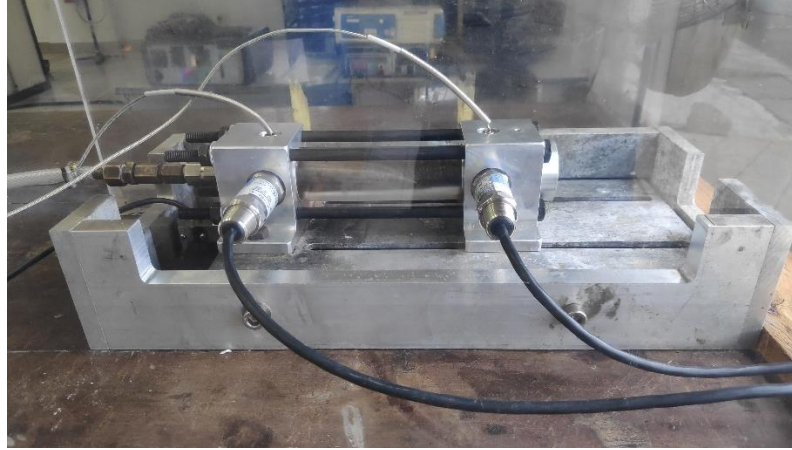


Figure 3.21 Experimental setup

### 3.4 DATA REDUCTION

The RT-5 technique, which is a reconstruction technique, was employed to calculate the O/F history. This technique involves solving an equation that includes the combustion efficiency,  $\eta$ , and the nozzle throat area,  $A_t$ .

$$\eta c^*(O/F, P_c) = \frac{P_c A_t}{\dot{m}_o (1 + \frac{1}{O/F})} \quad (20)$$

The average characteristic exhaust velocity,  $c_{ave}^*$ , is determined using Eq. (21), which allows for the calculation of O/F' according to Eq. (22).

$$c_{ave}^* = \frac{\int_0^{t_f} P_c A_t dt}{\int_0^{t_f} \dot{m}_o dt + M_f} \quad (21)$$

$$O/F' = \frac{\dot{m}_o c_{ave}^*}{P_c A_t - \dot{m}_o c_{ave}^*} \quad (22)$$

By inputting O/F' into the CEA code and assuming a relationship between  $\eta$  and O/F as given by Eq. (20), the equation for O/F can be solved.

$$O/F = \frac{\dot{m}_o \eta c_{th}^*(P_c, O/F)}{P_c A_t - \dot{m}_o \eta c_{th}^*(P_c, O/F)} \quad (23)$$

Figure 3.22 shows the calculation flowchart for RT5 according to Okuda et al. (2020).

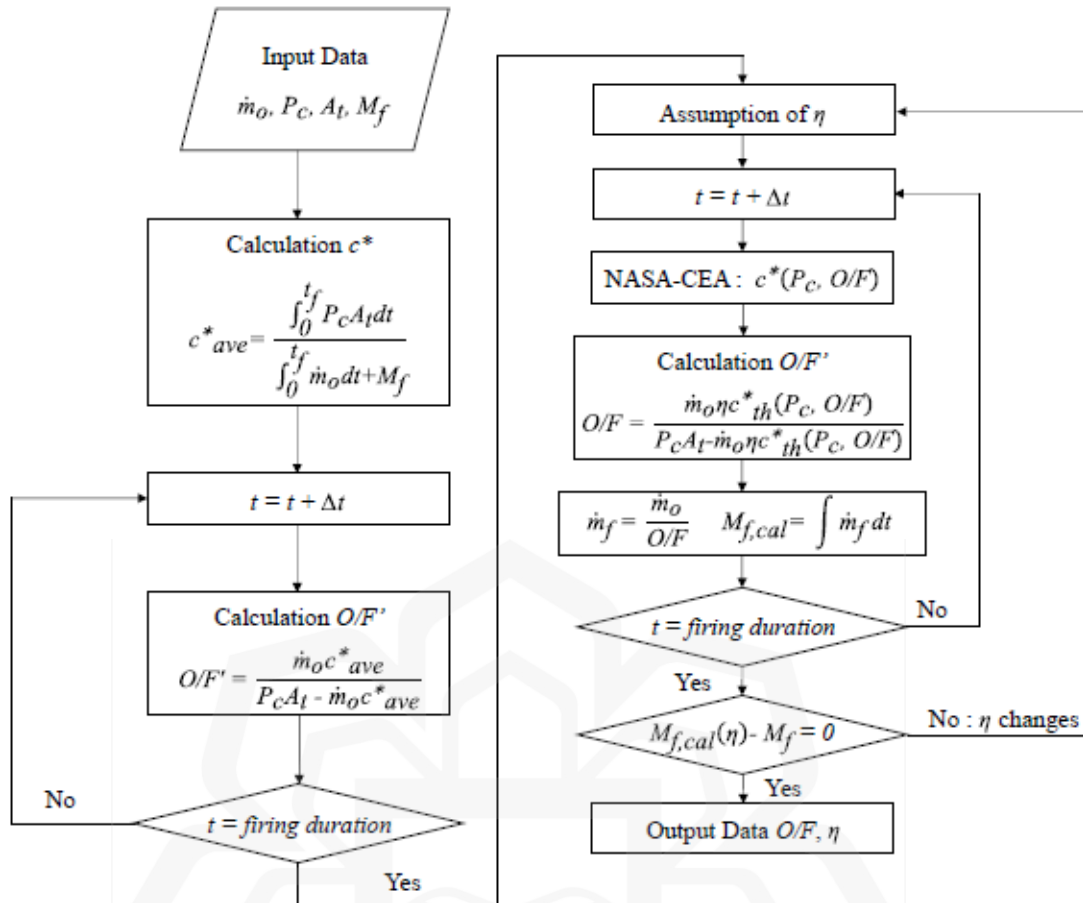


Figure 3.22 Calculation flowchart for RT5 (Okuda et al., 2020)

### 3.5 THEORETICAL PERFORMANCE ANALYSIS OF HIGH ENTROPY ALLOYS

Various HEA concentrations and oxidisers were evaluated in this study. Table 3.8 lists the many HEAs that are employed. These HEA were tested for how concentration in PW affected the metrics of propulsive performance. Oxidants such as GOX, LOX, N<sub>2</sub>O, hydrogen peroxide (H<sub>2</sub>O<sub>2</sub>), dinitrogen tetroxide (N<sub>2</sub>O<sub>4</sub>), and inhibited red fuming nitric acid (IRFNA) were mixed with these fuels. The test was also conducted with varied O/F and chamber pressure to investigate their impact on the parameters governing propulsive performance. The free NASA CEA software was used to do thermochemical simulations. A variety of assumptions are made during the computation of the performance characteristics for rocket motors, including:

- zero velocity at the inlet of the combustion chamber
- homogeneous mixture

- complete combustion
- no heat loss
- one-dimensional flow
- isentropic expansion of the gases along the nozzle

The simulation investigation in this project opted for the equilibrium condition, which typically leads to higher values. This choice was made to capture a more comprehensive combustion of the paraffin droplets within the oxidizing flow. By considering the post-combustion zone, where complete combustion occurs, an equilibrium model can better represent the combustion process. This approach enables a more accurate analysis and understanding of the combustion behavior of PW in the hybrid rocket system.

The equilibrium condition was selected for this work because it represented an appropriate approximation to determine the upper limits of performances anticipated for the examined propellants. There were three separate test sets: 1) HEAs of different compositions, 2) HEA concentrations between 1 and 10 wt.% with O/F values between 1 and 3, and 3) various oxidisers. All the simulations were done at 344.74 kPa in the combustion chamber with PW as the base fuel. The criteria for each test are shown in Table 3.9.

Table 3.8 Composition of FeCoNiAl(1-x)B<sub>x</sub>Si HEA powders

Sample	Composition (wt.%)					
	Fe	Co	Ni	Al	B	Si
HEA1	0.27	0.27	0.27	0.05	0.05	0.10
HEA2	0.27	0.27	0.27	0.00	0.10	0.10

Table 3.9 Test conditions

Test	O/F	HEA Concentration [wt.%]	HEA	Oxidiser
1	2	1-10	HEA1,2	O <sub>2</sub>
2	1.0-3.0	1-10	HEA2	O <sub>2</sub>
3	1.0-3.0	1	HEA2	GOX, LOX, N <sub>2</sub> O, H <sub>2</sub> O <sub>2</sub> , N <sub>2</sub> O <sub>4</sub> , IRFNA

### 3.6 CONCLUDING REMARKS

The preliminary design and experimental setup were covered in this chapter. Hybrid rocket fuel is designed based on the requirements. The eight crucial parts are thoroughly detailed and analysed, including the rocket casing, fuel grain, nozzle, feeding system, ignition system, caps, test stand, and data acquisition system. The calculation of O/F and characteristic exhaust velocity's efficiency were also discussed in this chapter.

## **CHAPTER 4**

### **RESULTS AND DISCUSSION**

#### **4.1 INTRODUCTION**

The findings from the experiments and analytical calculations are presented in this chapter. The design's thermochemical characteristics and mission analysis help understand and provide a general summary of the experimental data. As indicated in Chapter 3, a single circular port is employed throughout the experiment, and the same design is compared with the analytical analysis. Firstly, the analytical study is validated using the case study having the same fundamental decisions listed for the preliminary design. Then, the calculation is compared with the experimental result during the steady state.

The results of the experiments using metal additives are then presented to analyse how using HEAs at various fuel masses, mass flux, and concentration affects the regression rate. Parameters like thrust, temperature, and pressure are collected with specialised equipment using a data acquisition module.

#### **4.2 FIRING TEST RESULTS**

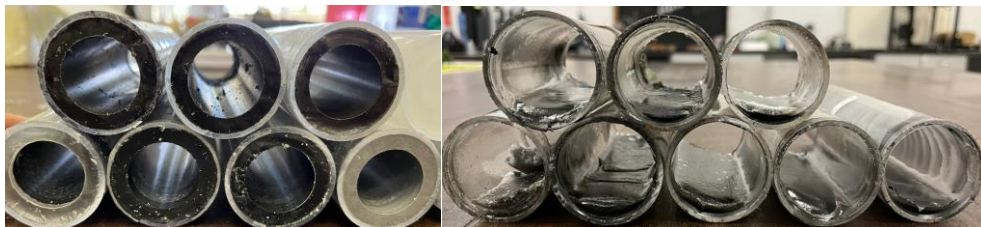
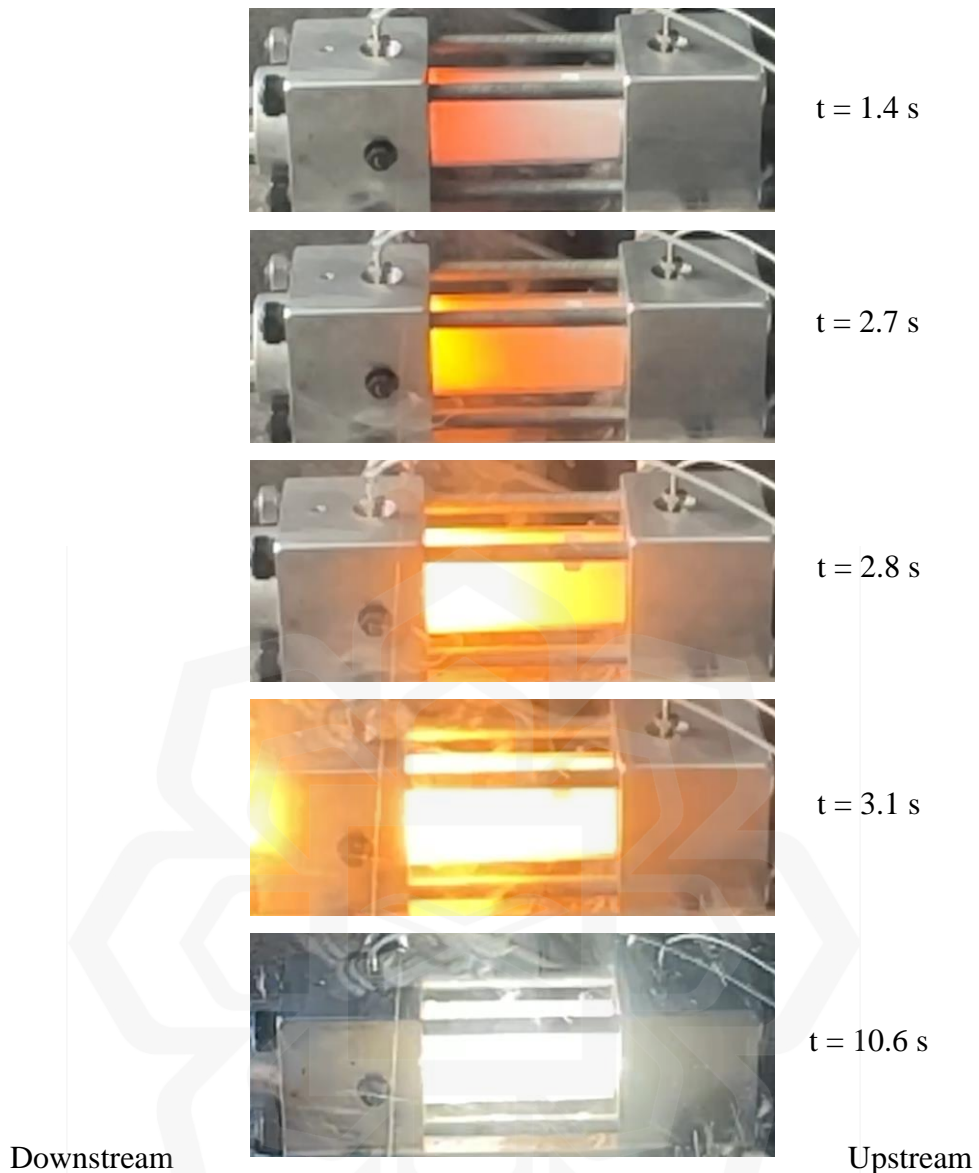
A total of nine firing tests were performed using GOX, where the oxidiser mass flux, fuel mass, and HEAs concentrations were varied. Tests 2 to 9 employed a single port end-burning hybrid rocket (EBHR). Test 1 was conducted using conventional combustion, while Test 9 utilized only polymethyl methacrylate (PMMA) as the fuel. Table 4.1 provides an overview of the test conditions for all the experiments.

Table 4.1 Test conditions

Test	Mass flux [kg/m <sup>2</sup> s]	Initial PW mass [kg]	HEAs [wt.%]
1	77.85	0.10	3
2	77.85	0.10	3
3	77.85	0.05	3
4	77.85	0.15	3
5	54.87	0.10	3
6	95.46	0.10	3
7	77.85	0.10	5
8	77.85	0.10	7
9	77.85	0.10	0

Figure 4.1 displays a series of time-marching images captured during Test 9 of the study, showcasing the combustion chamber. The nozzle is positioned on the left side. These images depict the progressive development of the diffusion flame starting from the end of the fuel and extending upstream. The combustion reached steady state after 10 seconds of firing. Figure 4.2 provides a comparison of the fuel before and after combustion.





The most important information from these firing experiments is summarised in Table 4.2, including firing time, chamber pressure, temperature, fuel mass flow

rate, thrust, the effectiveness of characteristic exhaust velocity, O/F, regression rate, and specific impulse. The efficacy of characteristic exhaust velocity and O/F was calculated using a data reduction approach known as RT5.

Table 4.2 Firing results

Test	$t_b$ [s]	$P_c^*$ [MPa]	$T_c^*$ [K]	$\dot{m}_f$ [g/s]	$F^*$ [N]	$\eta$ [-]	O/F*	$\dot{r}^*$ [mm/s]	$I_{sp}^*$ [s]
1	15.7	0.589	1296.8	2.7	58.91	0.781	1.750	3.59	118.65
2	18.7	0.536	1100.3	2.0	50.69	0.728	1.768	2.73	103.41
3	18.0	0.422	710.8	1.0	33.13	0.494	1.773	1.34	69.00
4	13.0	0.594	1244.5	4.2	59.66	0.893	1.732	5.58	116.75
5	17.0	0.377	1077.0	1.8	26.25	0.737	1.710	2.37	75.28
6	17.0	0.701	1255.0	2.4	76.09	0.751	1.738	3.24	126.77
7	15.4	0.592	1296.8	2.9	59.36	0.796	1.742	3.94	118.97
8	14.0	0.542	1079.8	3.1	51.62	0.771	1.787	4.17	103.16
9	14.6	0.500	959.3	2.0	45.15	0.703	1.787	2.70	92.20

\*Average values throughout the steady-state region of firing

The results show an increase of 44.32% and 52.75% in regression rate for fuel with 5% and 7% HEA concentrations, respectively, compared to the baseline of 3%. HEA concentrations affect the fuel mass flow rate of the HRM while the initial mass of the fuel has the most impact on the regression rate, with an increase of 104.4% for 50% more fuel mass compared to the baseline. However, the HRM with the highest specific impulse is the one with a rise of 22.62% mass flux compared to the baseline. Figures 4.3 and 4.4 show the chamber pressure, temperature, regression rate, and thrust for every firing.

The highest thrust and specific impulse are obtained in Test 6, with the highest mass flux. In contrast, the highest regression rate is obtained in Test 4, which has the highest initial fuel mass. The lowest thrust is from Test 5, which has the lowest mass flux, while Test 3, which has the least initial fuel mass, has the lowest specific impulse and regression rate. From the figures below, it shows that mass flux has the most

influence on the exit pressure, which significantly affect the performances of the HRM.

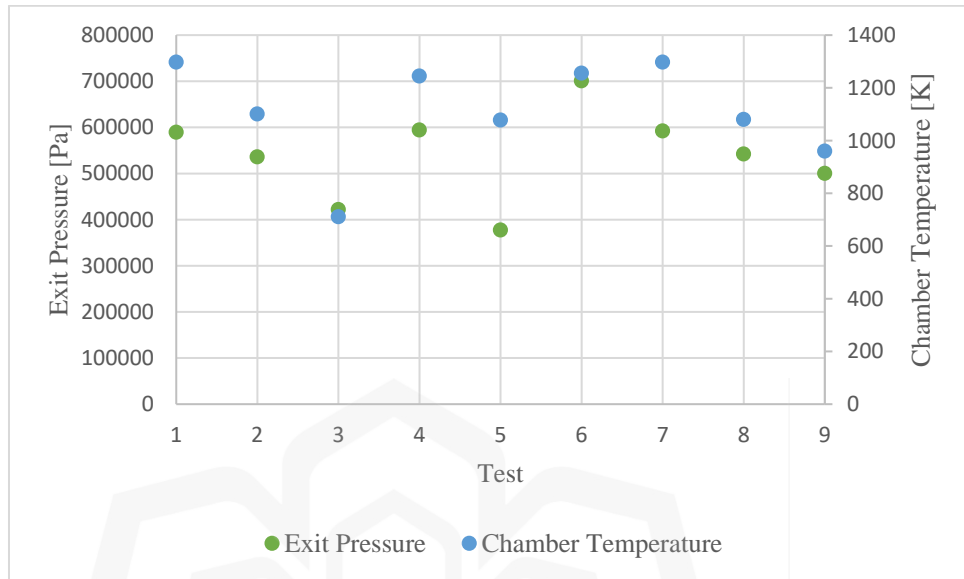


Figure 4.3 Chamber pressure and temperature for each test



Figure 4.4 Regression rate and thrust for each test

Figures 4.5-4.8 present the histories of chamber pressure and oxidiser mass flow rate, respectively, for Test 2 and Test 6. It can be observed that during steady-state chamber pressure conditions in both Tests, the O/F histories remain relatively constant. This is due to the constant fuel surface area throughout combustion. This

result agrees with other works on EBHR and confirms that end-burning can remove O/F fluctuations in HRM.

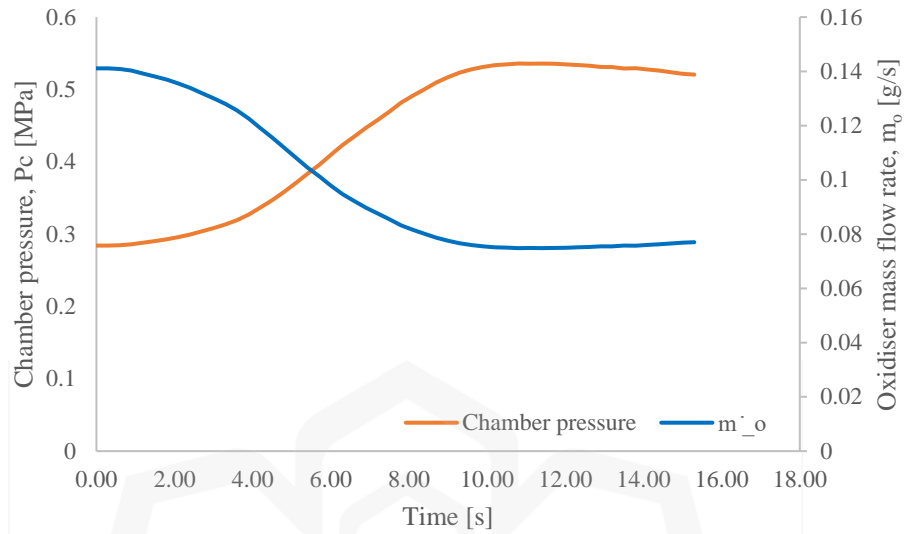


Figure 4.5 Histories of chamber pressure and oxidiser mass flow rate (Test 2)

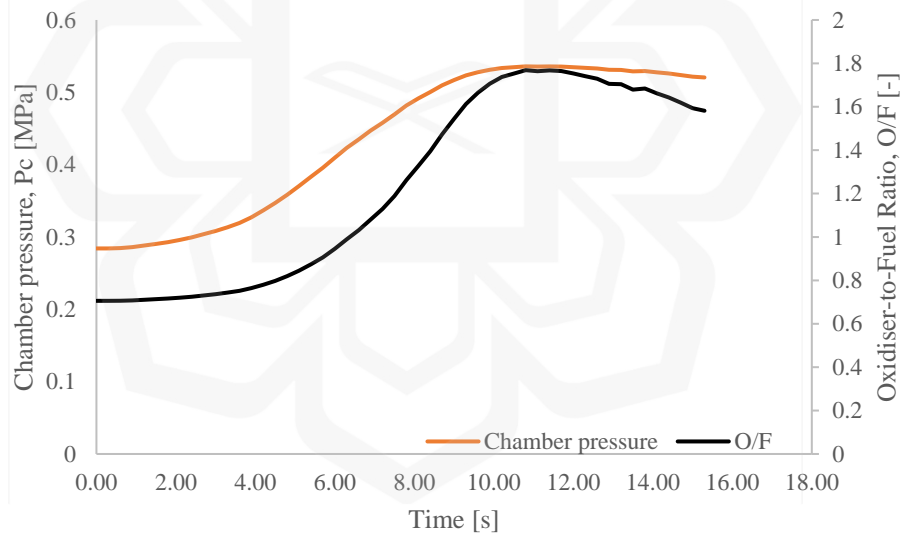


Figure 4.6 Histories of chamber pressure and O/F (Test 2)

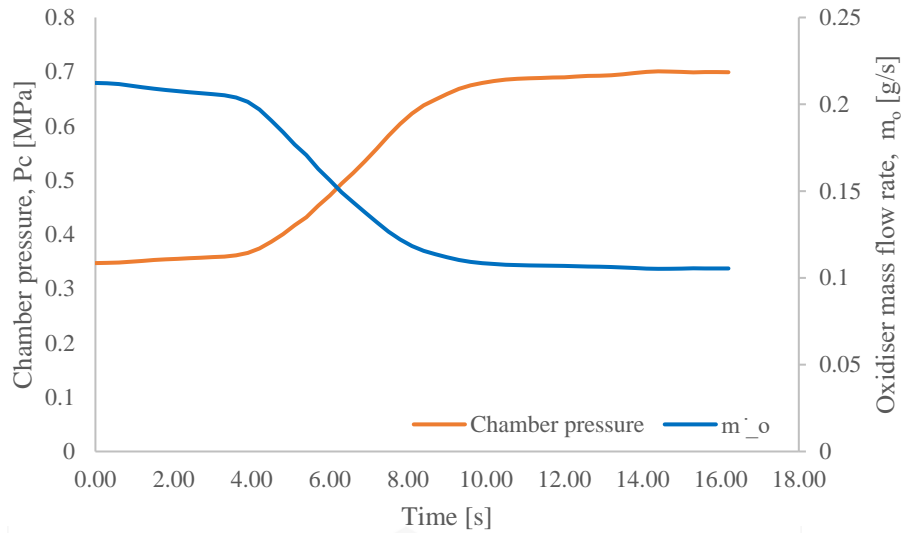


Figure 4.7 Histories of chamber pressure and oxidiser mass flow rate (Test 6)

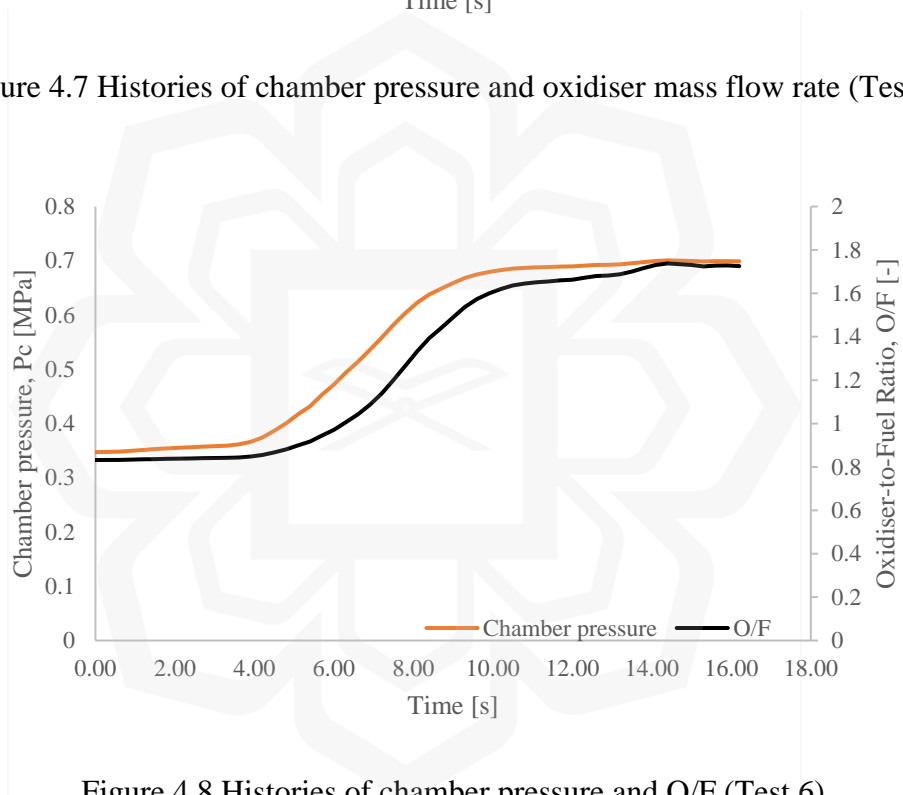


Figure 4.8 Histories of chamber pressure and O/F (Test 6)

### 4.3 FUEL REGRESSION CHARACTERISTIC

Figure 4.9 illustrates the correlation between the regression rate and chamber pressure. By applying the least-squares method, the empirical constants of the regression rate formula (Eq. 19) were obtained as  $n = 1.44$  and  $\alpha = 7.73$ , with a correlation coefficient of 0.575. This correlation coefficient indicates the relationship between the fuel regression rate observed during the tests and the curve depicted in Figure 4.7. It is

worth noting that the pressure exponent in this study's results significantly deviates from unity, which contrasts with previous research where pressure exponents were typically close to unity.

One possible explanation for this discrepancy is the absence of fuel regression in the stabilized combustion mode, which differs from the findings of earlier studies. This result aligns with the observations of Saito et al. (2019), who also found a positive correlation between the regression rate and chamber pressure in their previous investigations. The average regression rates in this study were 3.3, higher than the average of 2.9 observed in earlier studies utilizing gaseous oxygen as the oxidiser in single-port fuel configurations by Saito et al. (2019). The presence of HEAs in the fuel composition could contribute to these higher average regression rates.

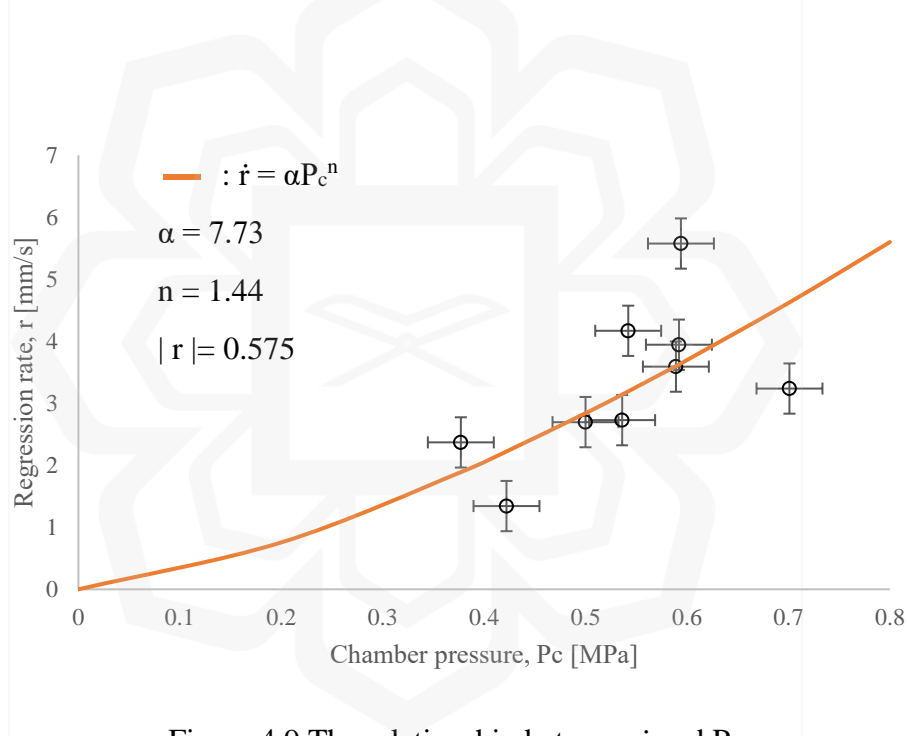


Figure 4.9 The relationship between  $\dot{r}$  and  $P_c$

#### 4.4 PRELIMINARY DESIGN ANALYSIS

The calculations from the preliminary design were compared to the experimental results as shown in Table 4.3. The analysis was done on Test 9 where there is no presence of HEA. The comparison shows low percentage errors for all the selected parameters especially with lower HEAs' concentration (Test 2, 3% HEA and Test 9, 0% HEA), which makes the calculations marginally acceptable to be used for

preliminary design of EBHR. The involvement of HEAs affect the properties of the fuel, resulting in less accurate calculations as the HEAs' concentration increases.

Table 4.3 Comparison of results between preliminary design and experiment

Parameter	Thrust [N]	Specific impulse [s]	Regression rate [g/s]
Preliminary Design	56.39	103.93	2.84
Experiment (Test 2)	50.69	103.41	2.73
Error [%]	11.24	0.5	4.03
Preliminary Design	62.79	116.67	3.01
Experiment (Test 7)	59.36	118.97	3.94
Error [%]	5.78	1.93	23.6
Preliminary Design	49.07	92.42	2.63
Experiment (Test 9)	45.15	92.2	2.7
Error [%]	8.68	0.24	2.59

#### 4.5 THEORETICAL ANALYSIS RESULTS

The results from the simulation were compared to the experimental results, as shown in Table 4.4 and Figure 4.10.

Table 4.4 Comparison of results between CEA-NASA and experiment

HEA Composition [wt.%]	CEA Thrust [N]	Experimental Thrust [N]	Percentage error [%]
0	58.09	45.15	22.27
3	71.00	76.09	7.18
5	58.64	59.36	1.22
7	58.44	51.62	11.67

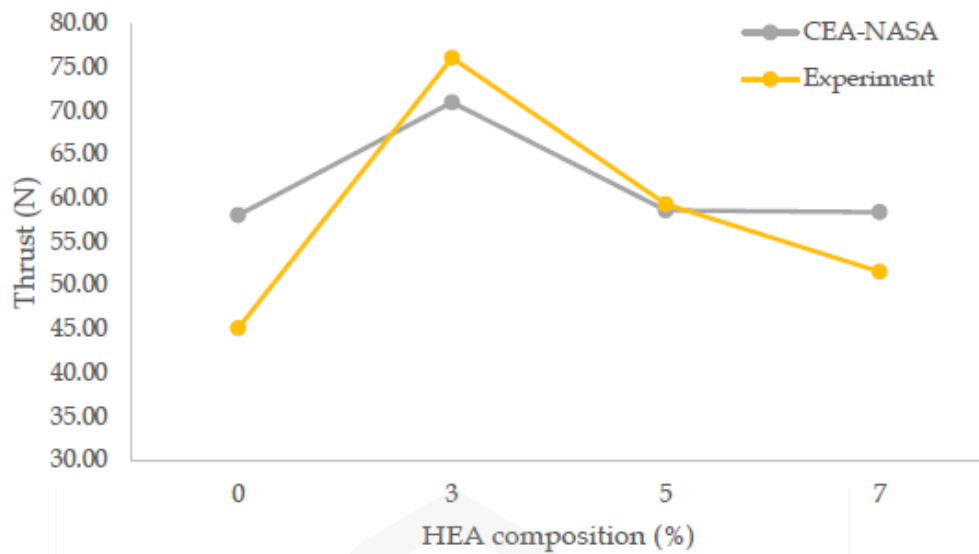


Figure 4.10 Comparison of results of CEA-NASA and experiment

Both results indicate a similar pattern in which 3% HEA provides the most thrust. Table 4.5 shows the performance difference between two different HEA compositions.

Table 4.5 Comparison of HEA1 and HEA2 with varying wt.% in PW

Concentration (wt.%)	c* [m/s]		I <sub>sp</sub> [s]		Temperature [K]	
	HEA1	HEA2	HEA1	HEA2	HEA1	HEA2
1	1749.1	1749.2	117.08	117.09	3162.82	3162.95
2	1745.5	1745.8	116.76	116.78	3168.76	3169.03
3	1741.8	1742.2	116.42	116.45	3174.41	3174.80
4	1738.0	1738.5	116.09	116.12	3179.80	3180.39
5	1734.1	1734.7	115.75	115.80	3184.91	3185.68
6	1730.0	1730.8	115.40	115.46	3189.74	3190.71
7	1725.9	1726.8	115.06	115.13	3194.29	3195.48
8	1721.6	1722.7	114.70	114.78	3198.55	3199.97
9	1717.2	1718.5	114.34	114.43	3202.54	3204.21
10	1712.8	1714.2	113.99	114.09	3206.24	3208.17



In every scenario, HEA1 with aluminium had somewhat worse performance than HEA2. Regarding characteristic velocity, specific impulse, and adiabatic flame temperature, HEA2 has an average improvement of 0.04%, 0.05%, and 0.03%, respectively compared to HEA1. This might be because HEA1, with a total latent heat of 126.9 J/g, is less thermally active than HEA2, which has a total latent heat of 136.34 J/g (Arifah et al., 2023) due to the higher reactivity of Boron in comparison to Aluminium (Nordin et al., 2022). Figure 4.11-4.13 shows the ideal values of characteristic velocity, specific impulse and adiabatic flame temperature that the thermochemical simulation produced for all HEA concentrations.

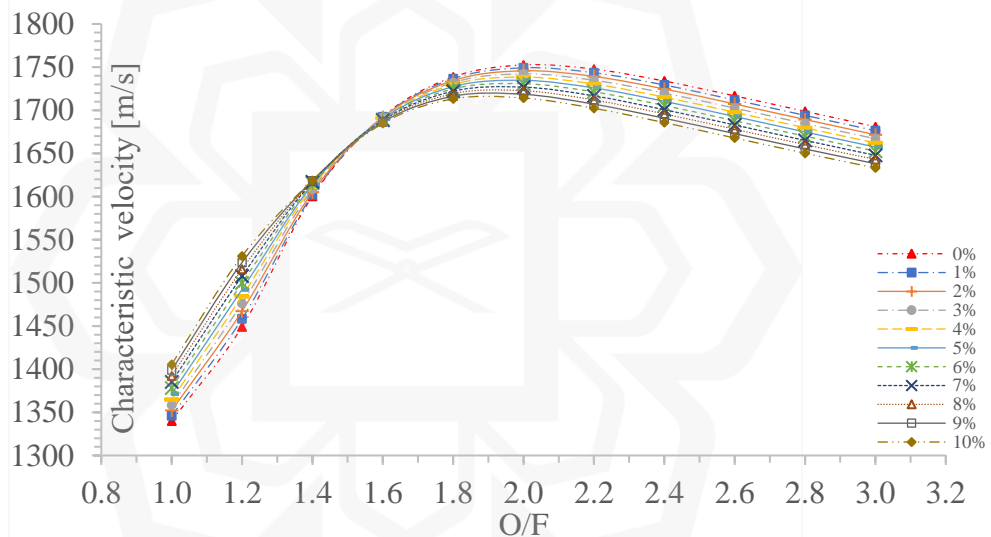


Figure 4.11 Characteristic velocity of the concentrations of HEA2 as a function of O/F

Every HEA concentration has a maximum characteristic velocity when the O/F is 2.0. The fuel with 0% HEA had the highest average characteristic velocity (1752.6 m/s), whereas fuel with 10% HEA had the lowest. After reaching an O/F of 1.4–1.6, the characteristic velocity of a higher HEA concentration begins to fall faster than that of a lower HEA concentration. For instance, during 1.0–1.4, the characteristic velocity of 10% HEA was higher than that of 9% HEA, but at 1.6–3.0, it dropped below the 9% HEA. The simulated specific impulse trend of the HEA concentrations versus O/F is depicted in Figure 4.12.

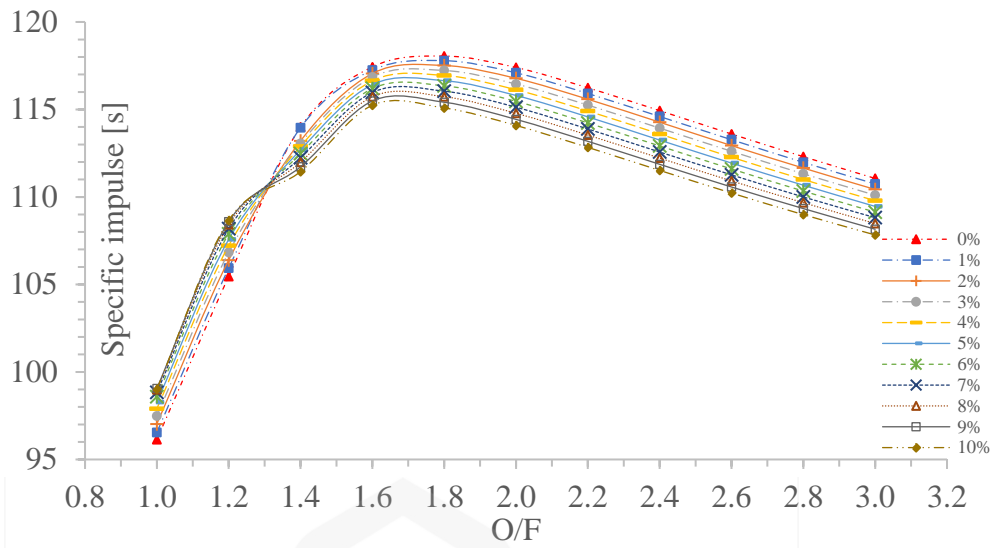


Figure 4.12 Specific impulse of the concentrations of HEA2 as a function of O/F

When the O/F is at 1.8, the specific impulse is maximum for all HEA concentrations. The fuel containing 0% HEA had the highest peak at 118.05 s, whereas the fuel containing 10% HEA had the lowest peak at 115.09 s. The specific impulse follows the same trajectory as the characteristic velocity, starting higher than the specific impulse of a lower HEA concentration but declining quicker after reaching an O/F of 1.3. The adiabatic flame temperature curve for various HEA concentrations is shown in Figure 4.13.

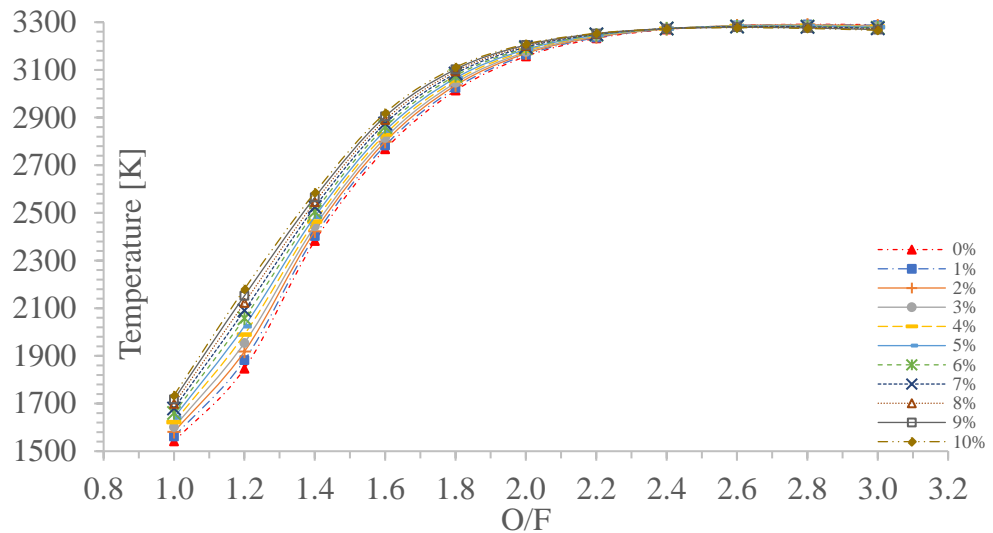


Figure 4.13 Adiabatic flame temperature of the concentrations of HEA2 as a function of O/F

When the O/F is between 2.6 and 2.8, the highest adiabatic flame temperature is reached for each HEA concentration. Although it has the lowest average temperature of 2825.02 K, the fuel with 0% HEA has the greatest peak temperature of 3291.4 K. The fuel containing 10% HEA had the highest average temperature of 2916.36 K but the lowest peak temperature of 3277.1 K. Although it happens later in the O/F, the adiabatic flame temperature trended in the same direction as the other metrics. Figure 4.14 shows the optimal values of characteristic velocity discovered using thermochemical modelling for all oxidants.

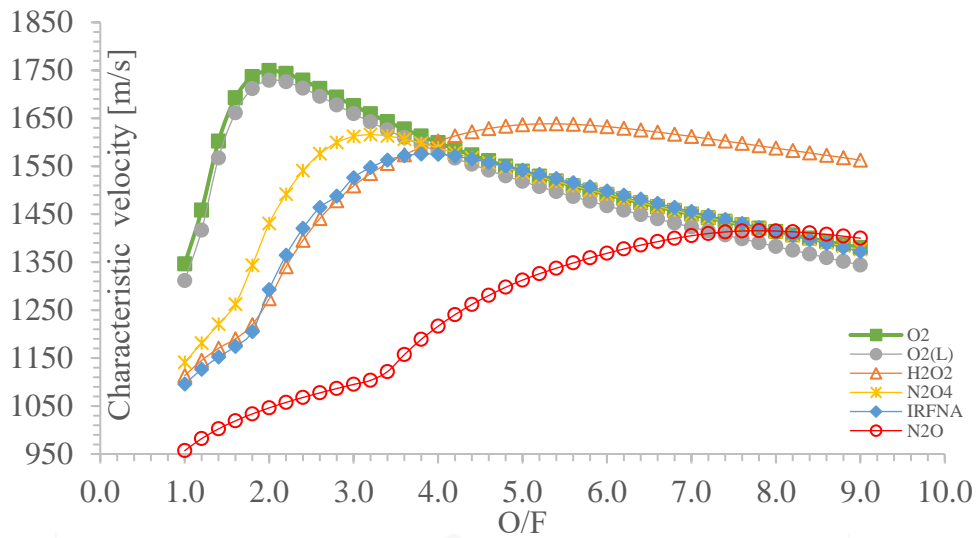


Figure 4.14 Characteristic velocity of the different oxidants as a function of O/F

When GOX is used as the oxidiser, the characteristic velocity is at its greatest, 1729 m/s, for an O/F of 2.0. The lowest peak value, however, was obtained when N<sub>2</sub>O was used as an oxidiser which was 1415.6 at an O/F of 7.8. The composition of combustion products that contain nitrogen which does not participate in the oxidation process while retaining some of the generated heat should be the primary cause (Tarifa & Pizzuti, 2019). The oxidiser's simulated specific impulse trend versus O/F is depicted in Figure 4.15.

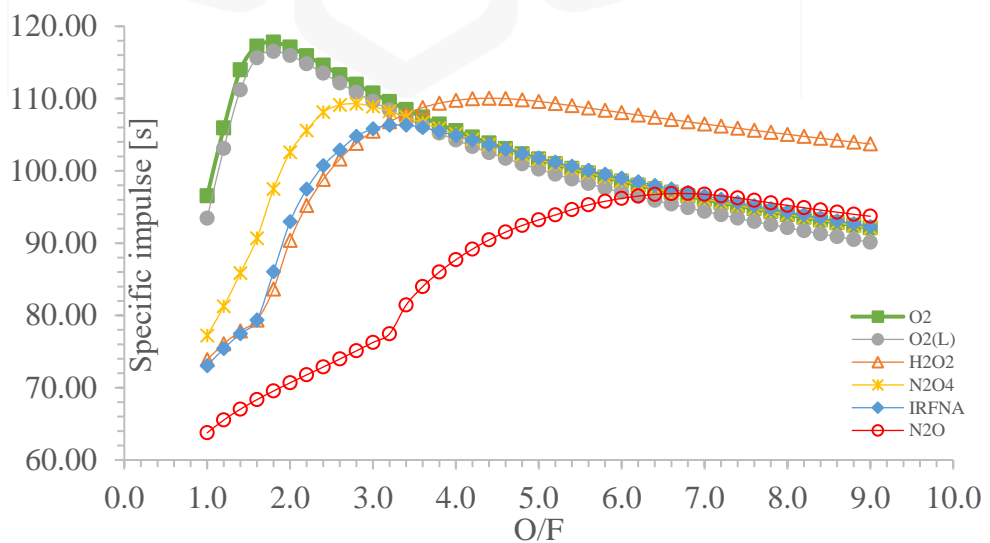


Figure 4.15 Specific impulse of the various oxidants as a function of O/F

With an O/F of 1.8, GOX exhibits the highest value of specific impulse, with a peak of 117.79 s. The lowest average specific impulse value comes from N<sub>2</sub>O, but it becomes higher than most oxidisers when reaching an O/F of 7.0. N<sub>2</sub>O<sub>4</sub> and IRFNA follow the same trend as GOX and LOX after reaching the peak value. The adiabatic flame temperature curve for the various oxidisers is shown in Figure 4.16.

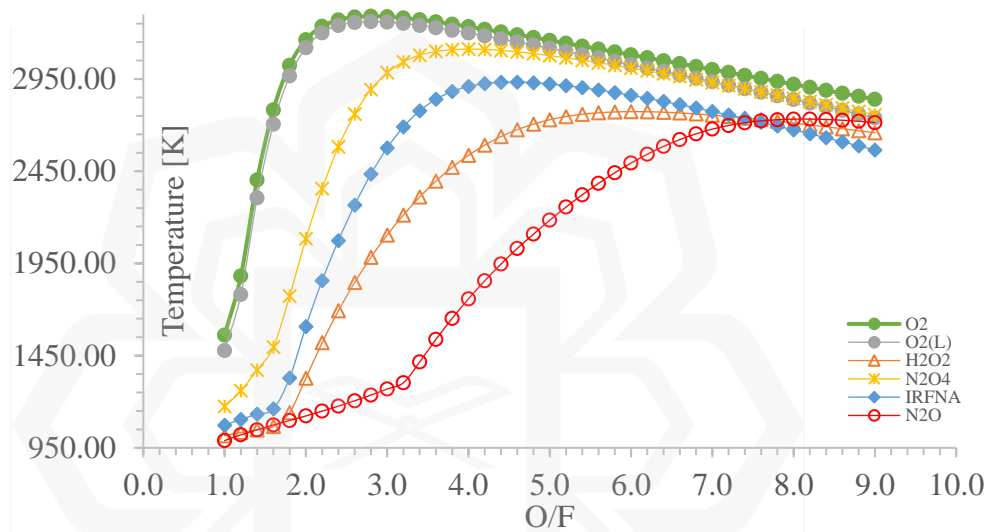


Figure 4.16 Adiabatic flame temperature of the various oxidants as a function of O/F

When GOX is used as the oxidiser, the highest temperature occurs at 3290.2 K with an O/F ratio of 2.8. Similarly, LOX yields temperature data with the same trend curve but a lower peak of 3261.2 K for the identical O/F. Up to an O/F of 1.8, the adiabatic temperatures of H<sub>2</sub>O<sub>2</sub> and N<sub>2</sub>O are comparable. While GOX and LOX optimise at lower O/F, H<sub>2</sub>O<sub>2</sub>, N<sub>2</sub>O<sub>4</sub>, IRFNA, and N<sub>2</sub>O tend to do so at higher O/F, which were 6.0, 4.0, 4.6, and 8.2, respectively. Figure 4.17 compares between this work and work done by Tarifa & Pizzuti (2019).

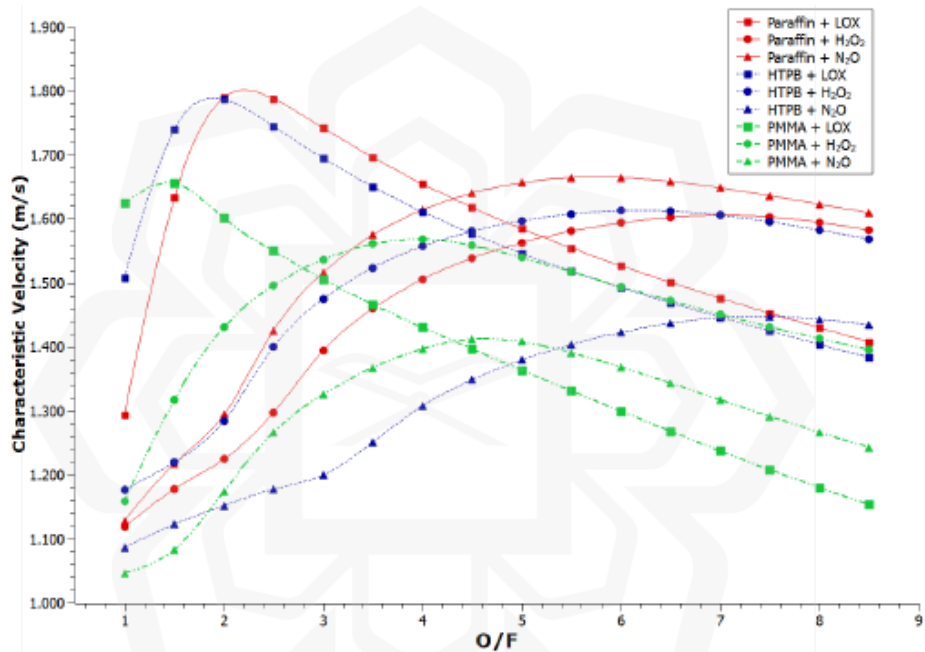
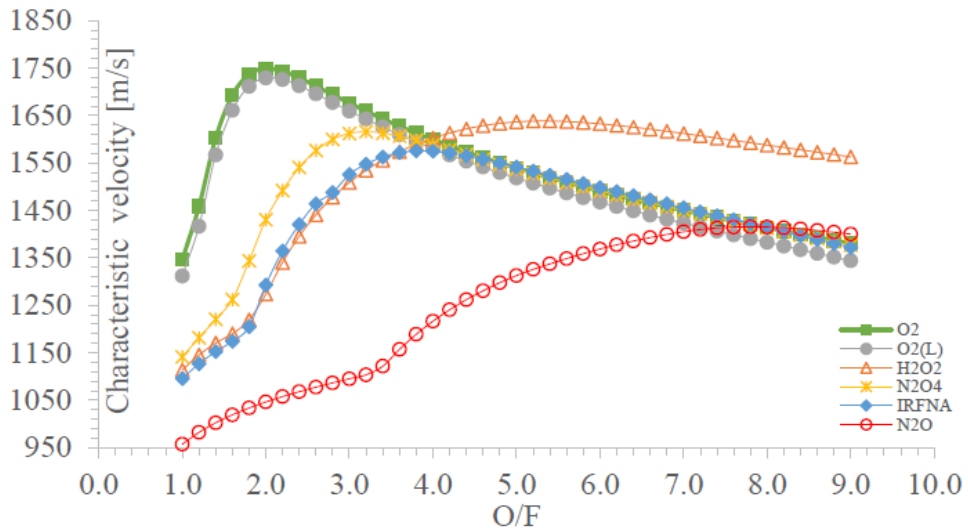


Figure 4.17 Comparison of characteristic velocity of various oxidants using CEA (Tarifa & Pizzuti, 2019)

#### 4.6 CONCLUDING REMARKS

This chapter covered the findings from Chapter 3. Nine static firings with various mass fluxes, initial fuel masses, and HEAs concentrations were carried out. From the static firings, the chamber's pressure, temperature, O/F, regression rate, thrust, and specific impulse were measured and studied. In this chapter, the outcomes of the theoretical analysis and preliminary design were also reviewed and contrasted with the experimental findings.

## CHAPTER 5

### CONCLUSION AND RECOMMENDATIONS

In conclusion, the research is about investigating EBHR doped with HEA. This research focuses on the propulsive performance of HEAs in HRM using the NASA CEA software and experimental results, which concentrate on the end-burning combustion mode. HEAs and lab-scaled static firings were successfully developed and conducted in the IIUM Propulsion Lab. There are several findings which can be listed here:

1. Conventional HRM performs better than the end-burning combustion in this study. This is due to the unstable combustion of the static firings.
2. There is little to no O/F shift in end-burning mode during steady-state pressure condition, which agrees with other previous works. The inclusion of HEAs as additives improve all the propulsive performance of the HRM.
3. The highest thrust and specific impulse was obtained from Test 6, which has the highest mass flux while the highest regression rate was from Test 4, which has the largest initial fuel mass.
4. The fuel regression and pressure exponent coefficient,  $a$  and  $n$ , was found to be  $= 7.73$  and  $1.44$ , respectively. These high values indicate that the regression rate of this HRM has a strong correlation to the chamber pressure.
5. A higher HEA percentage has better performance at lower O/F of 1.0-1.3 and perform worse the lower the HEA percentage becomes at higher O/F.
6. GOX presents the highest values, while  $N_2O$  provides the lowest values for all the propulsive parameters among the tested oxidisers when used with HEAs as additives.

The suggestions that are listed below will aid in improving the results of the analytical calculations and static firings.

1. Increasing the duration of combustion allows for the further accumulation of temperature and pressure, thereby extending the steady-state region.

2. Thorough examination and analysis of the preliminary design are necessary to improve the performance of the HRM.
3. Setting more precise initial conditions will allow further advancements in this study's data accuracy.
4. To improve the representation of the analytical results, the HEA and oxidiser properties can also be discussed in greater detail.





## REFERENCES

- Altman, D. (1991). Hybrid Rocket Development History. AIAA/SAE/ASME/ASEE 27th Joint Propulsion Conference.
- American Rocket Company (AMROC) records (no date) Homepage. Available at: <https://airandspace.si.edu/collection-archive/american-rocket-company-amroc-records/sova-nasm-2006-0047>.
- Ahn, B., Kang, H., Lee, E., Yun, Y., and Kwon, S. (2018). Design of multiport grain with hydrogen peroxide hybrid rocket. *Journal of Propulsion and Power*, 34(5), 1189–1197.
- Arifah, N., Mohamad, B., Hadi, A., Mohamaddiah, B., Hanafi, M., Azami, B., and Hidayah, N. (2023). Materials Today : Proceedings High entropy alloy as metal additive for hybrid rocket propellant. *Materials Today: Proceedings*, xxxx.
- Azami, H. (2014). Enhancement Of Regression Rate In Hybrid Rocket Motor Using Various Techniques. 8(33), 44.
- Chiaverini, M. J., and Kuo, K. K. (2007). *Fundamentals of Hybrid Rocket Combustion and Propulsion* (K. L. Frank (ed.)). American Institute of Aeronautics and Astronautics, Inc.
- Dada, M., Popoola, P., Adeosun, S., and Mathe, N. (2019). High entropy alloys for aerospace applications. In *Aerodynamics*. IntechOpen.
- David, L. (2004, October 4). SpaceShipOne Wins \$10 Million Ansari X Prize in Historic 2nd Trip to Space. Retrieved January 10, 2012, from space.com: <http://www.space.com/403-spaceshipone-wins-10-million-ansari-prize-historic-2nd-trip-space.html>
- Fowler, G. (1989) *George Koopman dies in wreck; technologist for space was 44*, *The New York Times*. Available at: <https://www.nytimes.com/1989/07/21/obituaries/george-koopman-dies-in-wreck-technologist-for-space-was-44.html>.
- Gharat, A., & Hastak, V. (2022). Hybrid Rocket Propulsion Development and Application. *Graduate Research in Engineering and Technology*, January 2009, 54–57. <https://doi.org/10.47893/gret.2022.1125>
- Green, L. (1964). “Introductory Considerations on Hybrid Rocket Combustion,” *Heterogeneous Combustion*, *Progress in Astronautics and Aeronautics*, 451.
- Hitt, M. A. (2020). Additively manufactured axial-injection, end-burning hybrid motor regression rate study. *Journal of Propulsion and Power*, 36(3), 485–487.

- Hitt, M. A., and Frederick, R. A. (2017). Experimental evaluation of a nitrous-oxide axial-injection, end-burning hybrid rocket. *Journal of Propulsion and Power*, 33(6), 1555–1560.
- Humble, R.W., Henry, G.N. and Larson, W.J. (1995). *Space Propulsion Analysis and Design*. McGraw-Hill, New York.
- Jens, E. T., Cantwell, B. J., & Hubbard, G. S. (2016). Hybrid rocket propulsion systems for outer planet exploration missions. *Acta Astronautica*, 128, 119–130. <https://doi.org/10.1016/j.actaastro.2016.06.036>
- Karabeyoglu, A. M., and Evans, B. J. (2014). *Effect of “O/F Shift” on Combustion Efficiency*. 1–19.
- K, R. K., Kuznetsov, A., and Natan, B. (2003). Design of a Lab-scale Hydrogen Peroxide/Hydroxyl Terminated Polybutadiene Hybrid Rocket Motor . 39th AIAA/ASME/SAE/ASEE Joint Propulsion Conference & Exhibit. Alabama: AIAA.
- Larson, C. W., DeRose, M. E., Pheil, K. L., and Carrick, P. G. (1997). “High Pressure Combustion of Cryogenic Hybrid Fuels in a Lab-Scale Burner,” *1995 JANNAF Joint Propulsion Conference*, Combustion Propulsion Information Agency, Johns Hopkins Univ., Columbia, MD, 117–128.
- Lestrade, J. Y., Anthoine, J., Musker, A. J., and Lecossais, A. (2019). Experimental demonstration of an end-burning swirling flow hybrid rocket engine. *Aerospace Science and Technology*, 92, 1–8.
- Miwa, T., Tsuji, A., Okuda, R., Yokobori, S., Soeda, K., Kamps, L., and Nagata, H. (2020). Visualization of fuel regression rate in axial-injection end-burning hybrid rocket. *AIAA Propulsion and Energy 2020 Forum*, 1–11.
- Moore, G. E., and Berman, K. (1956). A Solid-Liquid Rocket Propellant System. *Journal of Jet Propulsion*, 26(11), 965–968. <https://doi.org/10.2514/8.7170>
- Nagata, H., Saito, Y., Ishiyama, T., Inada, Y., Wakita, M., and Totani, T. (2014). "Evaluations of Data Reduction Methods for Hybrid Rockets", 65th International Astronautical.
- Nagata, H., Teraki, H., Saito, Y., Kanai, R., Yasukochi, H., Wakita, M., and Totani, T. (2017). Verification firings of end-burning type hybrid rockets. *Journal of Propulsion and Power*, 33(6), 1473–1477.
- Nordin, N. H., Zhaoyuan, L., Goodall, R., & Todd, I. (2022). Theoretical critical metastability temperature to interpret phase formation in a lamellar-like-structured high entropy alloy. *Journal of Materials Research and Technology*, 18, 2519–2530. <https://doi.org/10.1016/j.jmrt.2022.03.104>
- Okninski, A., Kopacz, W., Kaniewski, D., and Sobczak, K. (2021). Hybrid rocket propulsion technology for space transportation revisited - propellant solutions and challenges. *FirePhysChem*, 1(4), 260–271.

- Okuda, R., Komizu, K., Tsuji, A., Miwa, T., and Fukada, M. (2020). *Fuel Regression Characteristics of Axial-Injection End-Burning Hybrid Rocket Using Nitrous Oxide*.
- Okutani, Y., Saito, Y., Kimino, M., Tsuji, A., Soeda, K., and Nagata, H. (2018). Investigation of regression rate under high-pressure in axial-injection end-burning hybrid rockets. *2018 Joint Propulsion Conference*, 1–10.
- Paccagnella, E., Barato, F., Pavarin, D., and Karabeyoglu, A. (2017). Scaling parameters of swirling oxidizer injection in hybrid rocket motors. *Journal of Propulsion and Power*, 33(6), 1378-1394.
- Pal, Y., Mahottamananda, S. N., Palateerdham, S. K., Subha, S., and Ingenito, A. (2021). Review on the regression rate-improvement techniques and mechanical performance of hybrid rocket fuels. *FirePhysChem*, 1(4), 272–282.
- Pastrone, D. (2012). Approaches to Low Fuel Regression Rate in Hybrid Rocket Engines. *International Journal of Aerospace Engineering*, 2012, 649753.
- Saito, Y., Kimino, M., Tsuji, A., Okutani, Y., Soeda, K., and Nagata, H. (2019). High pressure fuel regression characteristics of axial-injection end-burning hybrid rockets. *Journal of Propulsion and Power*, 35(2), 328–341.
- Sutton, G. P. (1992). *Rocket Propulsion Elements: An Introduction to the Engineering of Rockets* (6th ed).
- Sutton, G. P., and Biblarz, O. (2017). *ROCKET PROPULSION ELEMENTS* (9th ed.). John Wiley & Sons, Inc.
- Tarifa, M. C., and Pizzuti, L. (2019). *Theoretical Performance Analysis Of Hybrid Rocket Propellants Aiming At The Design Of a Test Bench And a Propulsive System*. 8.
- Travis, T. S. (2017). Introduction to Rocket Science and Engineering. In CRC Press Taylor & Francis Group (2nd ed., Vol. 3).
- Tsai, M., and Yeh, J. (2014). *High-Entropy Alloys : A Critical Review High-Entropy Alloys : A Critical Review*. June, 37–41.
- Vignesh, B., and Kumar, R. (2020). Acta Astronautica Effect of multi-location swirl injection on the performance of hybrid rocket motor. *Acta Astronautica*, 176(May), 111–123.
- Wongyai, P., and Greatrix, D. R. (2016). Regression rate estimation for swirling-flow hybrid rocket engines. *Journal of Propulsion and Power*, 32(1), 18–22.
- Zhang, W., Liaw, P. K., and Zhang, Y. (2018). *Science and technology in high-entropy alloys*.
- Zhao, B., Yu, N., Liu, Y., Zeng, P., & Wang, J. (2018). Unsteady simulation and experimental study of hydrogen peroxide throttleable catalyst hybrid rocket motor. *Aerospace Science and Technology*, 76, 27–36.